Chapter 5: Beam Measurement Results

In the preceding chapters we have discussed the experimental procedures used and given a framework for analysis of the data. We present below the results of our measurements, divided into two major categories:

- results for lattice strength up to the onset of detectable growth of beam emittance ($59° \leq \sigma_0 \leq 88°$).
- results for the range $\sigma_0 > 88°$, over which collective effects place a measurable lower bound on the beam emittance for a given current; or, conversely, an upper bound on the current that does not cause emittance growth.

We will informally use the descriptions "low-σ_0" for the first of these regions, and "high-σ_0" for the second. Beams with σ_0 below 59° are stable as checked at $\sigma_0 = 45°$, but these data are of very limited extent and of less interest and hence are not discussed here. Sources of error are discussed in Chapter 7.

5.1 Results for $\sigma_0 \leq 88°$

5.1.1 Focusing aberrations

The SBTE source is a solid-state source and produces a relatively uniform current density (see Fig. 5.1). There is a small spherical aberration, a deviation from linear optics, of only about 20% of the intrinsic width of the source distribution, detectable using the horizontal dimension source diagnostics (not shown). The only apparent consequence of this aberration is the higher current density at the edges of the beam as it exits the injector, as shown in Fig. 5.1. In general, aberrations in the focusing of the beam will result in distortions of the phase space contours from elliptical shapes, either by making the contours more square in shape or by distorting the contours

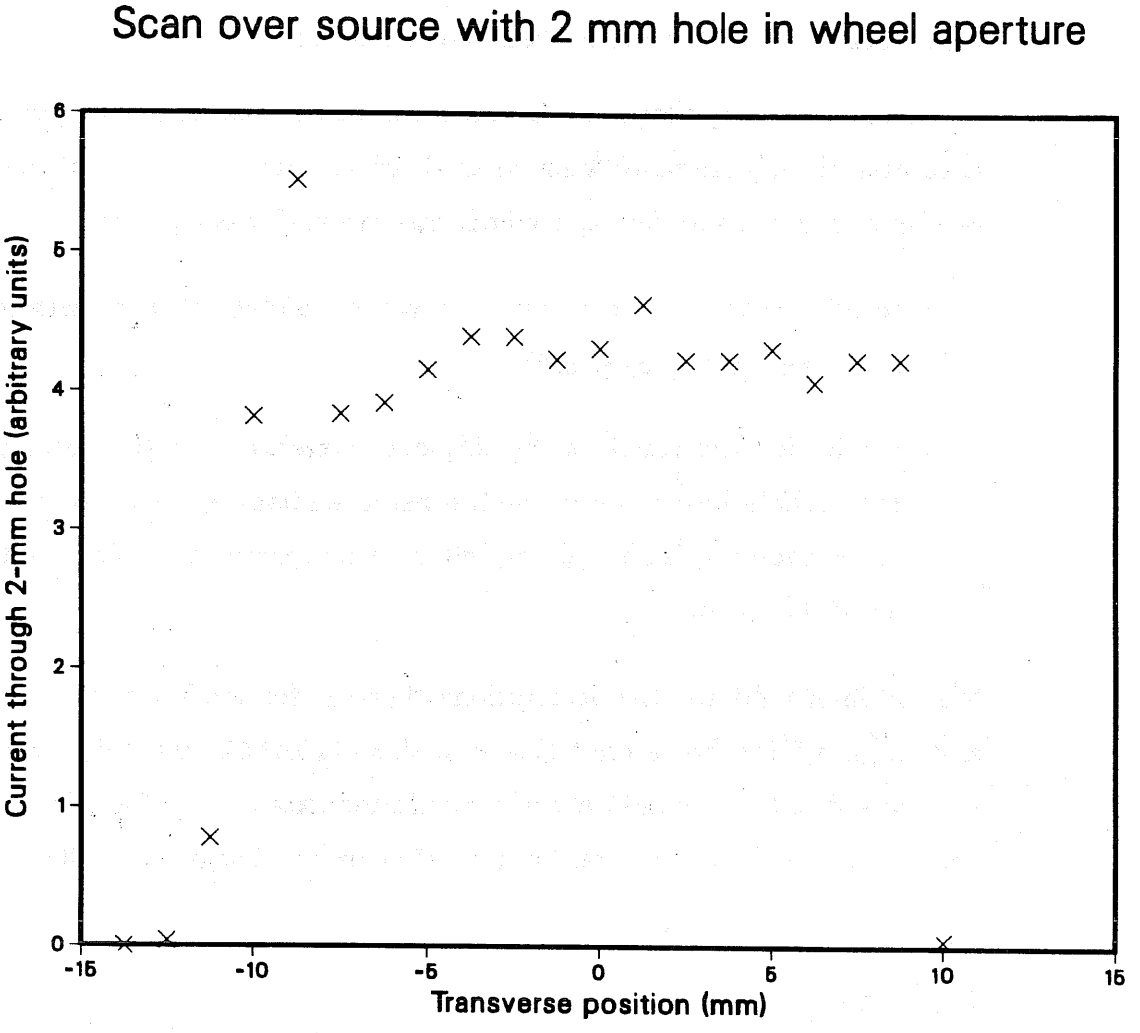

Figure 5.1: SBTE injector current density profile, measured using a 2-mm diameter aperture and scanning across the source at approximately the vertical center. The observed current density is relatively uniform over the beam diameter. The high point at the left of the figure is reproducible, and may be a result of the imperfect focusing of the injector on the beam. For other values of height that we could check, the beam profile was similar.

into an S-like shape. We will refer to aberrations as a property of the beam distribution (caused by aberrations in the overall focusing field), as well as being a property of the focusing field itself. More serious aberrations in the phase space distribution of the beam were noted downstream of the matching section. We show three sequences of phase space contours in Fig. 5.2. The four rows show measurements at, respectively, quadrupoles Q4, Q35, Q59, and Q80, in the horizontal dimension. For column (a), $\sigma_0 = 59°$. The minor distortion seen at Q4 is not visible in the downstream measurements. We infer that the slight S-like shape of the contours as measured at Q4 is due either to matching section aberrations or to the source distribution. In contrast, phase space contours for one $\sigma_0 = 83°$ matching attempt are shown in column (b) of the same figure. The distortion of the contours at Q4 is much more severe for $\sigma_0 = 83°$ than for $\sigma_0 = 59°$. The aberrations again are not evident in downstream measurements, although for the phase space distribution as measured at Q35, the contours surrounding most of the beam enclose an area appreciably greater than for the corresponding $\sigma_0 = 59°$ case. The aberration as measured at Q4 was visibly diminished by weakening the M1–M2 doublet, varying the other matching elements to maintain a matched beam (see Fig. 5.2c). In this figure, the voltages on the elements M1–2 were about 15% lower than for Fig. 5.2b.

5.1.2 Beam loss bounds

We could not measure the current of the beam as it exits the source, because of the restricted clearance and the geometry of the source housing. The first point along the lattice at which we could insert a deep cup for current measurement was after M5, the last matching quadrupole. We also had SFC's along the lattice at Q2, Q36, and Q60. For $59° < \sigma_0 < 83°$, with well-matched initial conditions, no loss of beam was detected between M5 and Q82, within

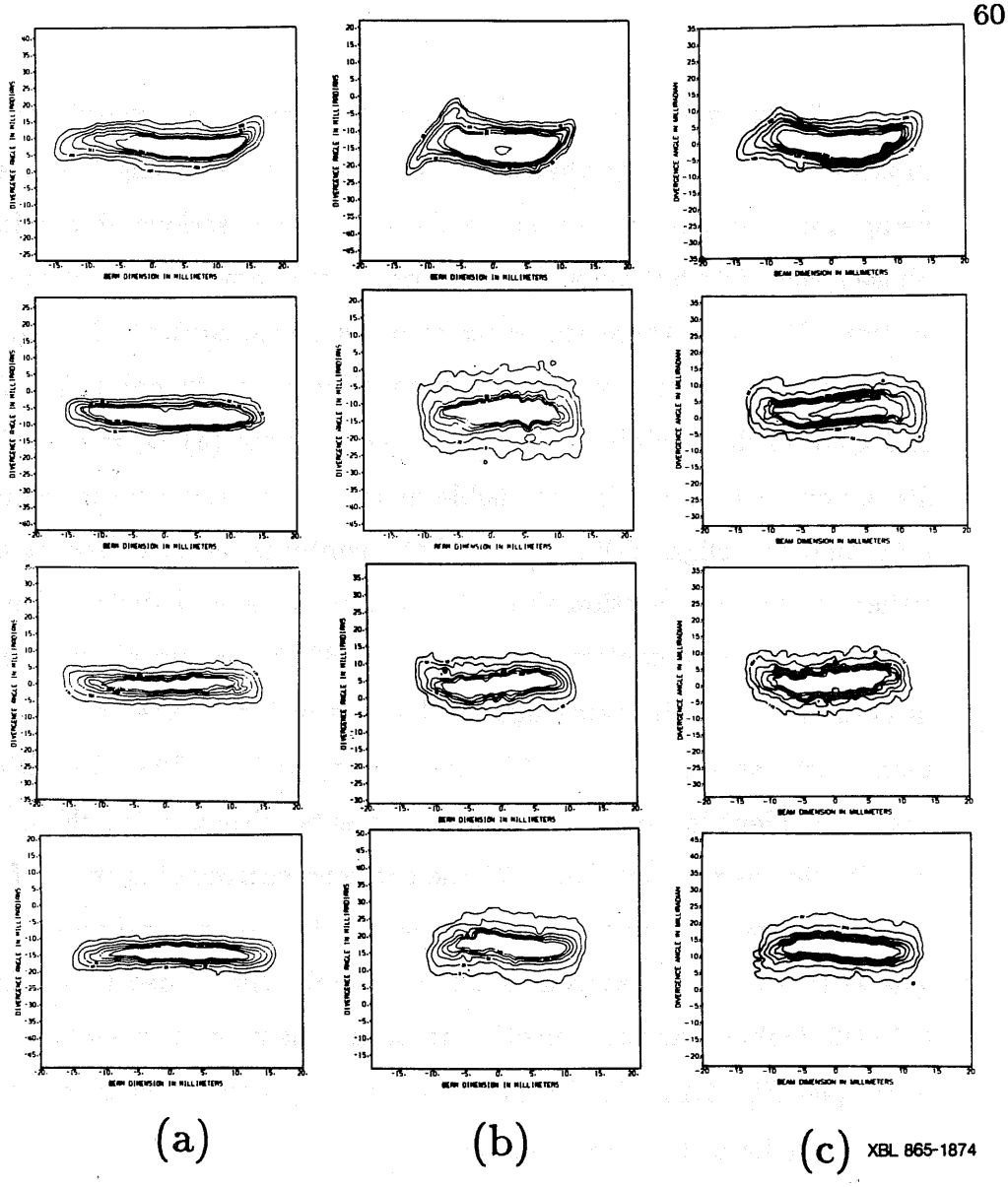

Figure 5.2: Focusing aberrations downstream of the matching section. The four rows are for measurements made, respectively, downstream of quadrupoles Q4, Q35, Q59, and Q80. (a) A sequence of measurements along the lattice for $\sigma_0 = 59°$. The aberration after Q4 is very small, and washes out during further transport. (b) An early set of measurements for $\sigma_0 = 83°$. The aberration at Q4 is much worse than for (a), but washes out during further transport. In this process, however, the low level contours in phase space appear to become diluted. (c) When we weaken the M1–2 doublet of the matching section, maintaining a matched beam by varying the other matching elements, the aberration measured for $\sigma_0 = 83°$ at Q4 is diminished. The broadening in the low-level contours in the downstream measurements also is not as pronounced.

the experimental precision of about 2%, by direct measurement on the cups. Fig. 5.3 shows DFC traces after M5 with various pulse-lengths compared to the DFC trace after Q82. The figure shows the discrete downward steps in current due to the light ion velocity difference from the cesium ions. The direct response of the DFC at M5 to the cesium component is the same, within about $\sim 3\%$, as for the DFC at Q82. We expect the measured current at Q82 to be 2–3% lower than at injection as a result of the Marx pulse droop (see section 4.2), and about 1–2% lower from background gas collisions (see section 6.3). By direct comparison between these identical cups, we are able to detect any beam loss of more than about 0.3 mA, but we find no beam loss at this level.

For the unattenuated SBTE beam, after we shortened the injector to raise the gun current, we found that the current delivered into the DFC at Q82 was not absolutely constant, but showed a slight dependence on σ_0. The deviations in measured current were at the limit of experimental uncertainty, at the 2% level. The current measured at the end of the lattice for our best $\sigma_0 = 59°$ match was 15.2 mA, while for the best $\sigma_0 = 78°$ match, we measured 15.5 mA. Although the current measured at the entrance to the transport channel varied by about the same amount between the two cases, the slightly higher current may be due in part to the phenomenon found by Brewer [18]. A boundary layer of particles at the periphery of the source is focused improperly by fields distorted from the ideal by imperfect boundaries. These particles pass through the beam and penetrate outside the bulk beam distribution. If the beam clearance in the aperture is too small, these particles will be lost against the quadrupoles. But if the aperture is increased (by increasing the focusing field, in this instance), then the particles will be retained. We took care during construction of the ion source to minimize any gaps between the surface of the ion emitter and the focusing electrode bound-

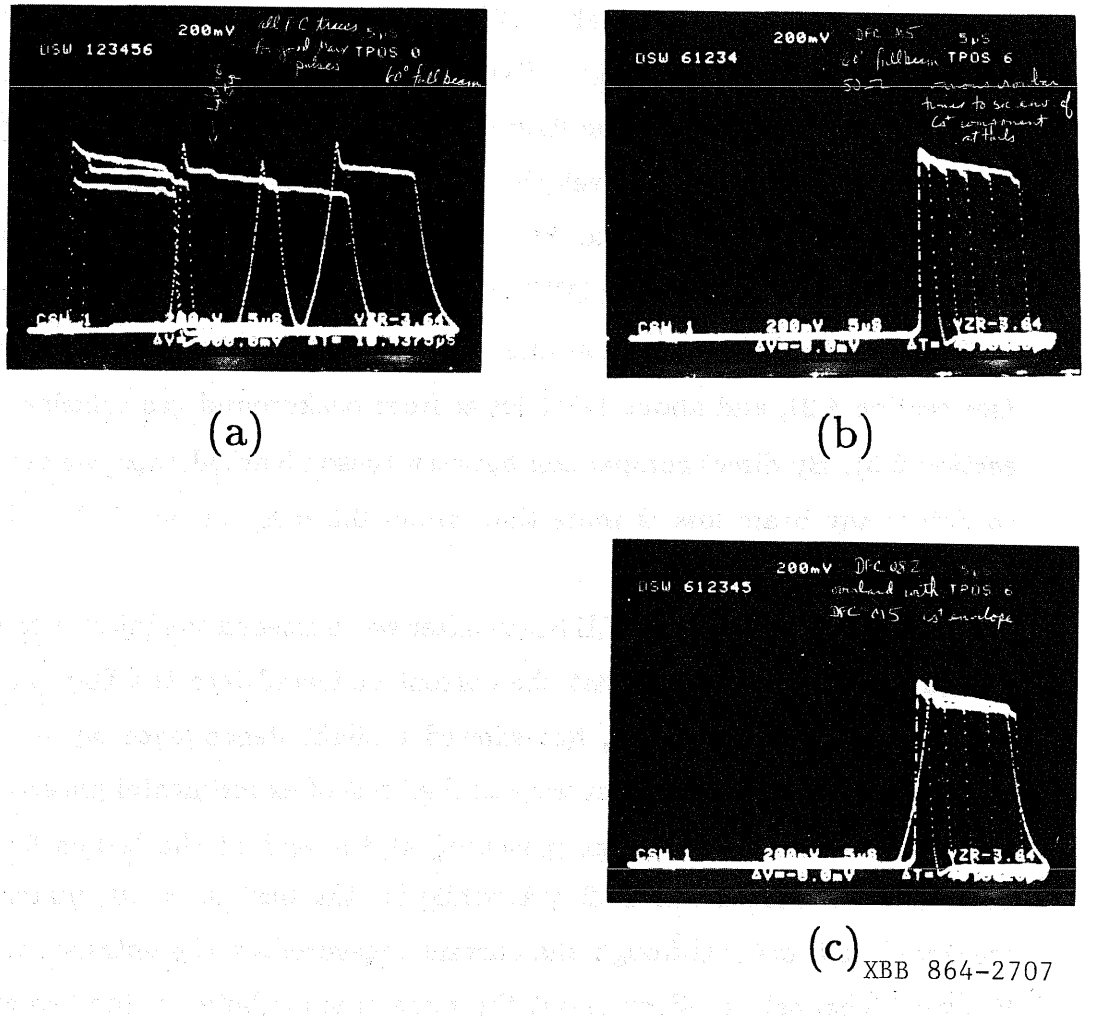

Figure 5.3: (a) Faraday cup traces along the lattice, showing the differences in the direct response to essentially equal beam currents. (b) Deep Faraday cup traces with short fall-times (at M5), showing the separation of the light ion component from the Cs^+ component in the small step at the trailing edge of the beam pulse before the main pulse ends. (c) Overlay of the Cs^+ component as measured at M5 and at Q82 using identical DFC's. The long fall-time at Q82 prevents observation of the undershoot at the tail of the pulse. The equality of Cs^+ component at either end of the lattice to within about 2% (the level of the beam loss from background gas interactions and beam debunching from the Marx generator output droop) may be seen from the oscilloscope traces. The effect of the longitudinal electric field is apparent from the elongation of the beam ends.

aries, but a small separation was necessary to avoid unnecessary conduction of heat away from the source. Two percent of the beam current corresponds to a boundary layer only 0.005 inches in width around the periphery of the 1-inch diameter source; this fraction of the beam could easily be subject to edge aberrations in the injector and be very difficult to identify in measurements on the beam.

Somewhat later, we provided for measuring charge accumulation on the quadrupoles, and we observed small beam-coincident currents. At this time, the injector grids had been altered, and the diagnostics needed for careful matching of the beam had been removed, so that we had no way of generating a well-matched beam. The ion beam spill current necessary to induce this signal, assuming a secondary electron gain factor of 15 (adjusted upward from 12 to make a crude allowance for field-enhanced and grazing incidence emission from the quadrupole surfaces), would have resulted in a 0.2 mA beam loss over the entire lattice if the loss were uniform in z. This was measured only at one location, half-way down the lattice and with a beam that had not been carefully matched. The signal was independent of pressure for low pressures, and thus was not due to background gas interactions. Loss of "translaminar" particles from the beam would provide a similar signal. These observations are from measurements at the limit of experimental uncertainty, and we believe that there is no collective mechanism involved to cause beam loss, given the existence of the mechanism described by Brewer.

5.1.3 Beam envelope measurements

We show some beam profile sequences for $\sigma_0 = 59°$ and $\sigma_0 = 83°$ in Fig. 5.4. As the strength of the lattice is raised, and the aberrations discussed in section 5.1.1 show up in the phase space measurements, the profile of the beam is also affected. By weakening the M1–2 doublet, the beam profiles are

smoothed near the injector. The beam profile is much smoother at the end of the lattice, as a result of dispersion of the space-charge oscillations.

Following the RMS envelope formalism, and denoting the RMS value of x as $\tilde{x}$, we plot $2\tilde{x}$ for the beam profiles of Fig. 5.4c and d, versus position along the lattice. The results are shown in Fig. 5.5. The value calculated from from the envelope equations is about 12 mm. (The measured beam size agrees very well with calculation using the envelope equations, as shown in Table 5.1 below. A set of data spanning the range of σ_0 used in these experiments from measurements at the end of the lattice is shown in Table 5.1 on page 82.) The profile data show initial transient oscillations quite clearly. Calculations of the frequencies of the simple envelope oscillation modes for the constant-focusing model are given in [40], and we have included some information in Ch. 2. The result for the symmetric breathing mode (apparent in Fig. 5.5 for the RMS radius of the beam) in terms of σ and σ_0 is given in Eqn. 2.9

$$k^2 = 2\sigma_0^2 + 2\sigma^2,$$

where k is the "wave-number" of the envelope oscillation, or $360°/\lambda$, where λ is the number of focusing periods in one wavelength of the oscillation. For this beam, $\sigma_0 \simeq 83°$ and $\sigma \simeq 16°$. The resulting wavelength of the envelope oscillation is very nearly three lattice periods, in very good agreement with the data. When we replaced the 45° parallel-wire grid used to terminate the injector with a 0.125-in cell-size honeycomb grid, the beam profile near the injector became much smoother, so we attribute the major part of these beam oscillations to perturbations due to the parallel-wire grid.

Although the RMS envelope oscillation is substantially dissipated by the time the beam has reached Q73 (see Fig. 5.4), the third moment of the beam distribution persists, with the beam still "sloshing" from side to side as it progresses down the channel. This mode of oscillation is visible also in

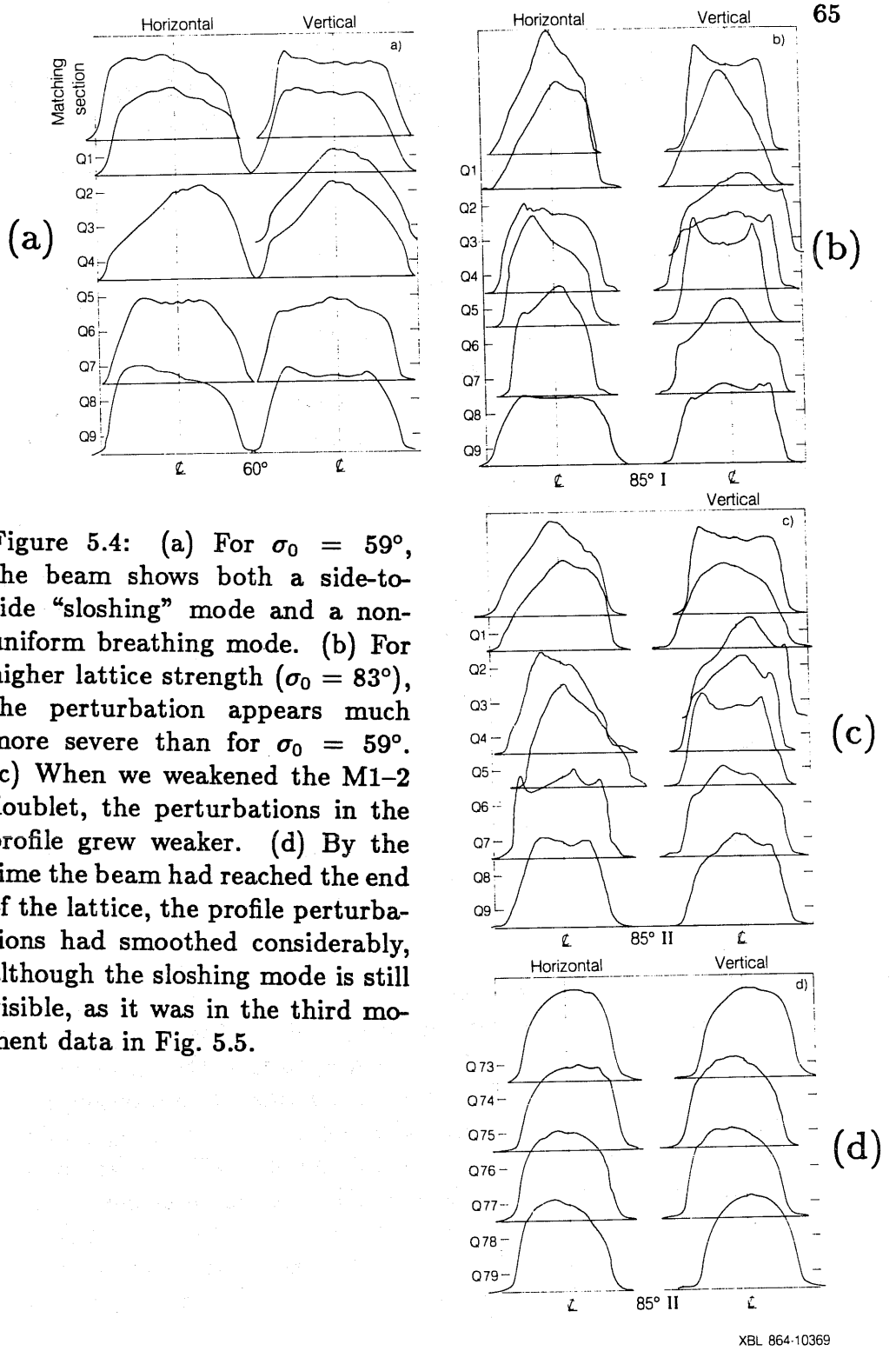

Figure 5.4: (a) For $\sigma_0 = 59°$, the beam shows both a side-to-side "sloshing" mode and a non-uniform breathing mode. (b) For higher lattice strength ($\sigma_0 = 83°$), the perturbation appears much more severe than for $\sigma_0 = 59°$. (c) When we weakened the M1–2 doublet, the perturbations in the profile grew weaker. (d) By the time the beam had reached the end of the lattice, the profile perturbations had smoothed considerably, although the sloshing mode is still visible, as it was in the third moment data in Fig. 5.5.

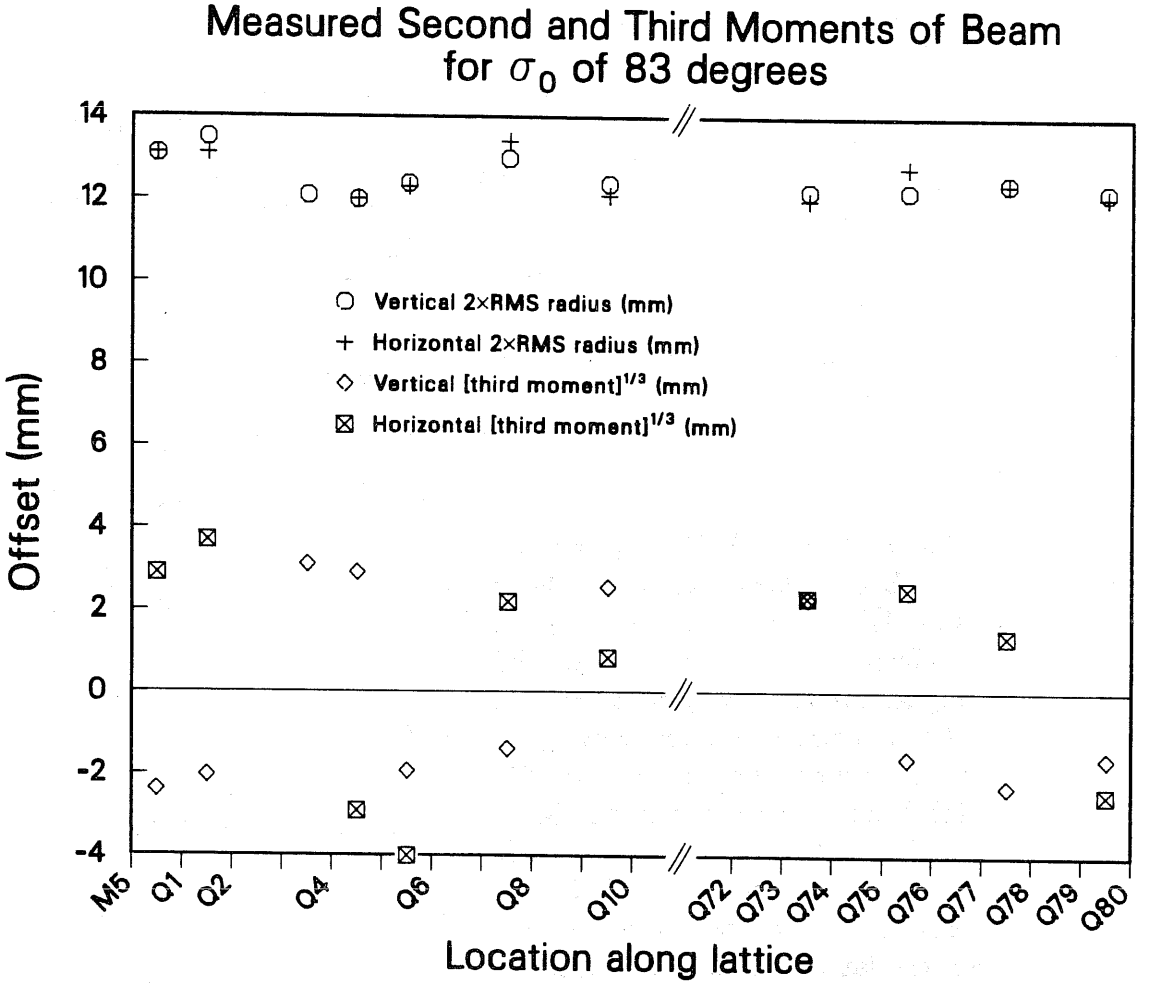

Figure 5.5: The points near the top of the figure show the measured RMS beam radius along the lattice for $\sigma_0 = 83°$. The envelope oscillation in the two planes is almost exactly in phase, so that the envelope oscillation with these initial conditions is in only one mode. The wavelength, λ in units of focusing periods, calculated from the smooth focusing model is such that $(360°/\lambda)^2 = 2\sigma_0^2 + 2\sigma^2$. For $\sigma_0 = 83°$ and $\sigma \sim 16°$, λ given by this formula is about three focusing periods, which is in good agreement with the measurements. The third moment of the beam distribution is plotted along the lower portion of the figure. The period of the oscillation is in reasonable agreement with the value $360°/\sigma_0$, as it should from constant-focusing calculations for σ much less than σ_0.

the profiles for M5–Q9, and we have included it in Fig. 5.5 by plotting the third moment of the beam profile along the lattice. We made no detailed comparison of the frequency of these oscillations with theoretical predictions, but we note that in the limit of a cold beam, there is a sextupole-symmetry oscillation with a non-zero third moment, with frequency degenerate with σ_0 [15]. The wavelength of such an oscillation for $\sigma_0 \sim 83°$ is about four focusing periods, which is consistent with the observations in Fig. 5.5.

5.1.4 Phase Space Measurement Results

For $\sigma_0 < 88°$, we saw no growth of emittance along the lattice for the current and emittance range experimentally accessible. Results for many measurements in the range $59° \leq \sigma_0 \leq 83°$ showed a nearly constant emittance downstream from the matching section. There is a slight consistent decrease in the RMS emittance for 95% of the beam particles as the beam passes through the lattice. The decrease is in the range 5–10%, and may be due in part to some systematic effect, such as achieving better slit alignment near the end of the lattice. Loss of the outer 2% of the beam could have a similar result. The slope of the i vs. $\epsilon(i)$ curve, which is a measure of the phase space density of the beam, remains nearly unchanged. The emittance versus current for the highest-intensity $\sigma_0 = 59°$ beam we could obtain from our source is shown in Fig. 5.6. When plotted on linear scales, the bulk distribution has a nearly linear current vs. emittance relationship. In the tails of the distribution, the I vs. ϵ curve breaks over, reflecting the low density of the tail.

As we attempted to match the beam into stronger lattices, the emittance measured after Q4 grew larger, because of the aberrations mentioned in section 5.1.1. The emittance was constant or decreased alightly along the lattice at the higher value for $\sigma_0 \leq 88°$, and we attribute the higher emittance down-

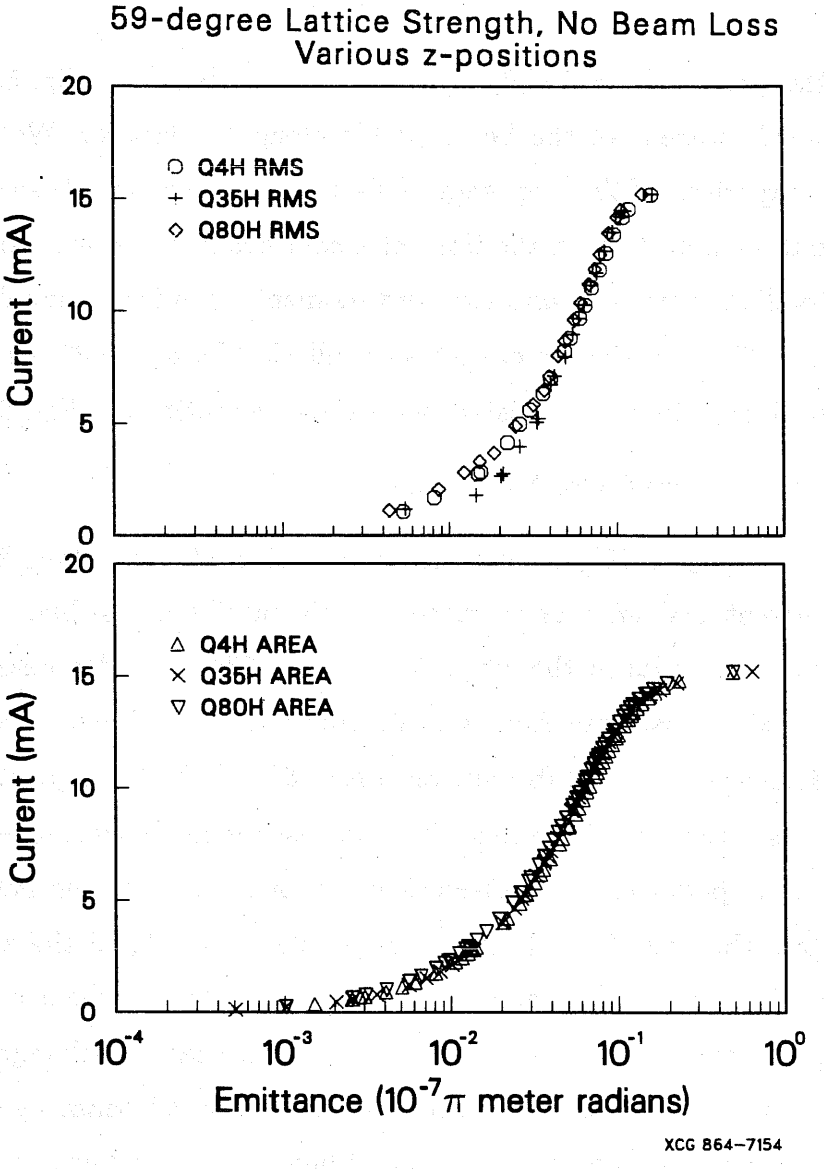

Figure 5.6: Plot of i vs. $\epsilon(i)$ for $\sigma_0 = 59°$. (a) RMS analysis of emittance, and (b) Area emittance. The distribution is almost linear for $i/I < 0.9$ when plotted on linear scales. In these and the succeeding figures 5.7 and 5.8, there is no perceptable change in the overall emittance. In the actual phase space data, however, there is a small tail of ions, with a density on the order of 1% of the peak value of the distribution, which forms outside the main beam. This is to be expected from realistic distributions, as a result of thermal tails in the distribution.

stream of the matching section in these cases to the matching section fields. Figs. 5.7 and 5.8 display the effect on the beam of raising the lattice strength. The area emittance curves show a growth for $\epsilon(I)$ as σ_0 rises, but not much variation along the lattice.

The only measurements we made using a lattice weaker than 59° were for $\sigma_0 = 45°$. These measurements were all made during the manual data acquisition period, with poor resolution, but we saw no evidence of emittance growth. This is in accordance with our belief that one cannot get into trouble by weakening the lattice if the beam is stable for $\sigma_0 = 59°$.

At about the $\sigma_0 = 88°$ level, with $\sigma \sim 16°$–$18°$, a small, persistent current loss began to occur, of about 4%. This lattice strength is in fact the stability limit for the most intense beam we could produce. Even a 6% increase in lattice voltage, corresponding to a σ_0 of about 94°, resulted in a 30% current loss at the Q82 DFC and a rapid rise in the emittance of the beam, as shown in Fig. 5.28. This marks the presently detectable onset of collective instability for space-charge dominated beams. The variation with lattice strength of the beam current transmitted to the DFC downstream of Q82 for $\sigma_0 \simeq 90°$ is shown in Fig. 5.9. The beam was matched for $\sigma_0 = 88°$, with a matched beam radius between quadrupoles of approximately 12 mm. The drop in current for low quadrupole voltage is due to mismatch of the beam.

5.2 Discussion of Results for $\sigma_0 \leq 88°$

5.2.1 Low-emittance limits

Theoretical predictions based on K-V model beams have indicated several mechanisms for emittance growth. Analogous to the $\sigma_0 = 180°$ single particle resonance with the focusing lattice, there are higher-order resonances possible for $\sigma_0 \geq 180°/n$ for $n \geq 2$. The envelope instability for $\sigma_0 \geq 90°$ is one such mode, for $n = 2$. The various oscillation modes for the K-V beam

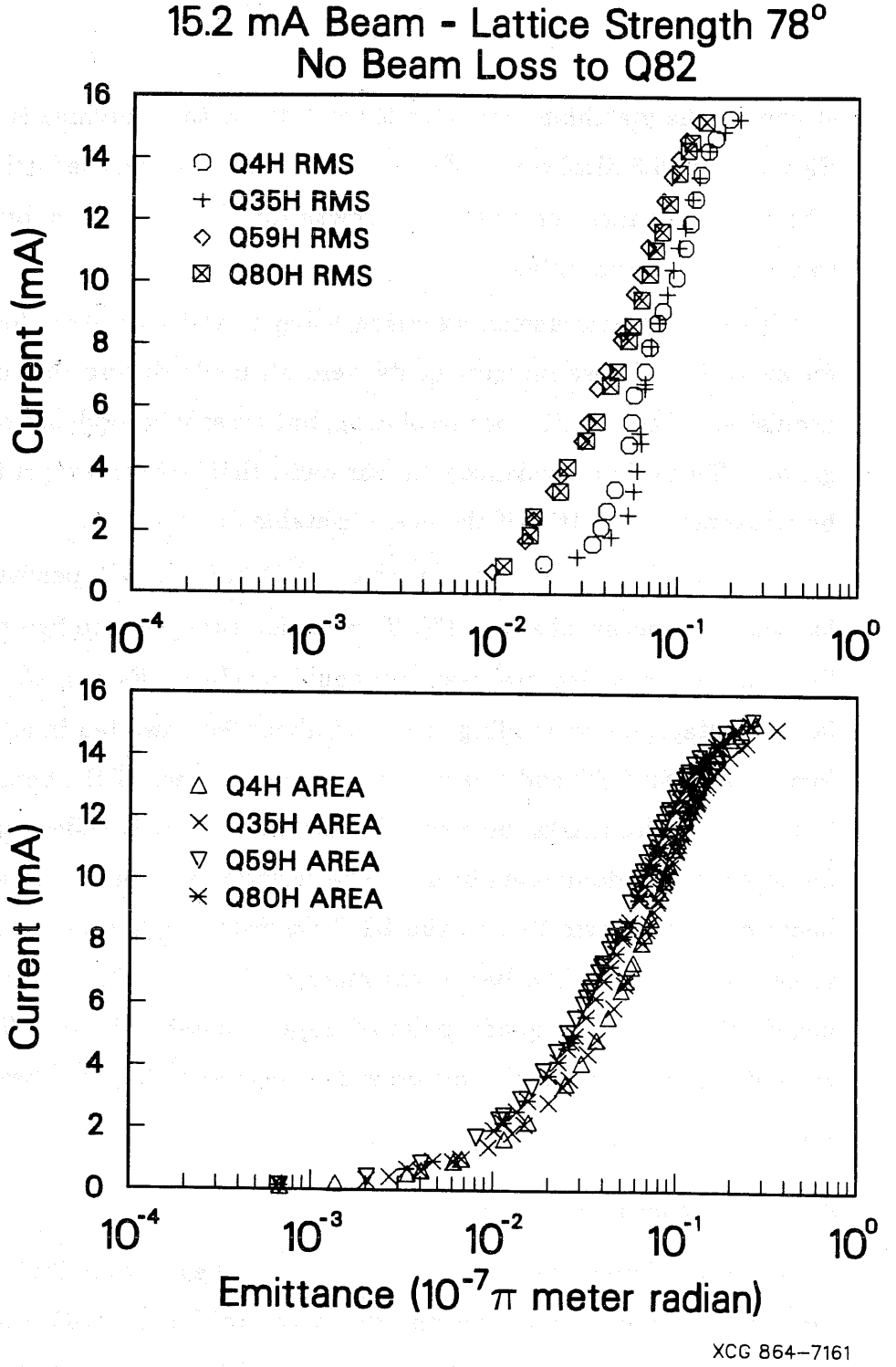

Figure 5.7: Integrated area and RMS emittances in the horizontal dimension for 15 mA beam, $\sigma_0 = 78°$.

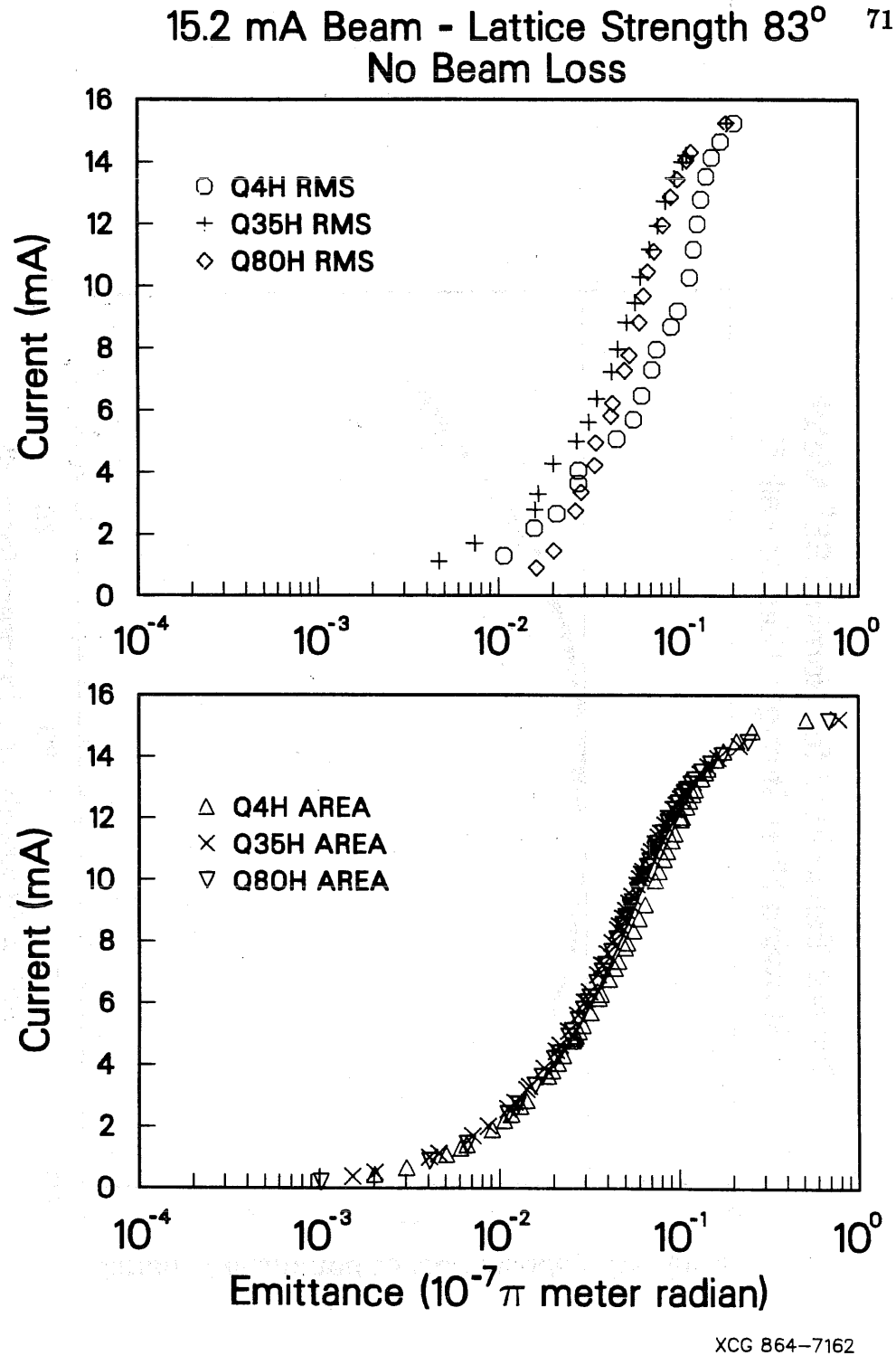

Figure 5.8: Integrated area and RMS emittances for 15 mA, $\sigma_0 = 83°$. The phase space contours are particularly distorted for the Q4 measurements (see Fig. 5.2c), which results in higher values for the RMS emittance there than for the downstream measurements.

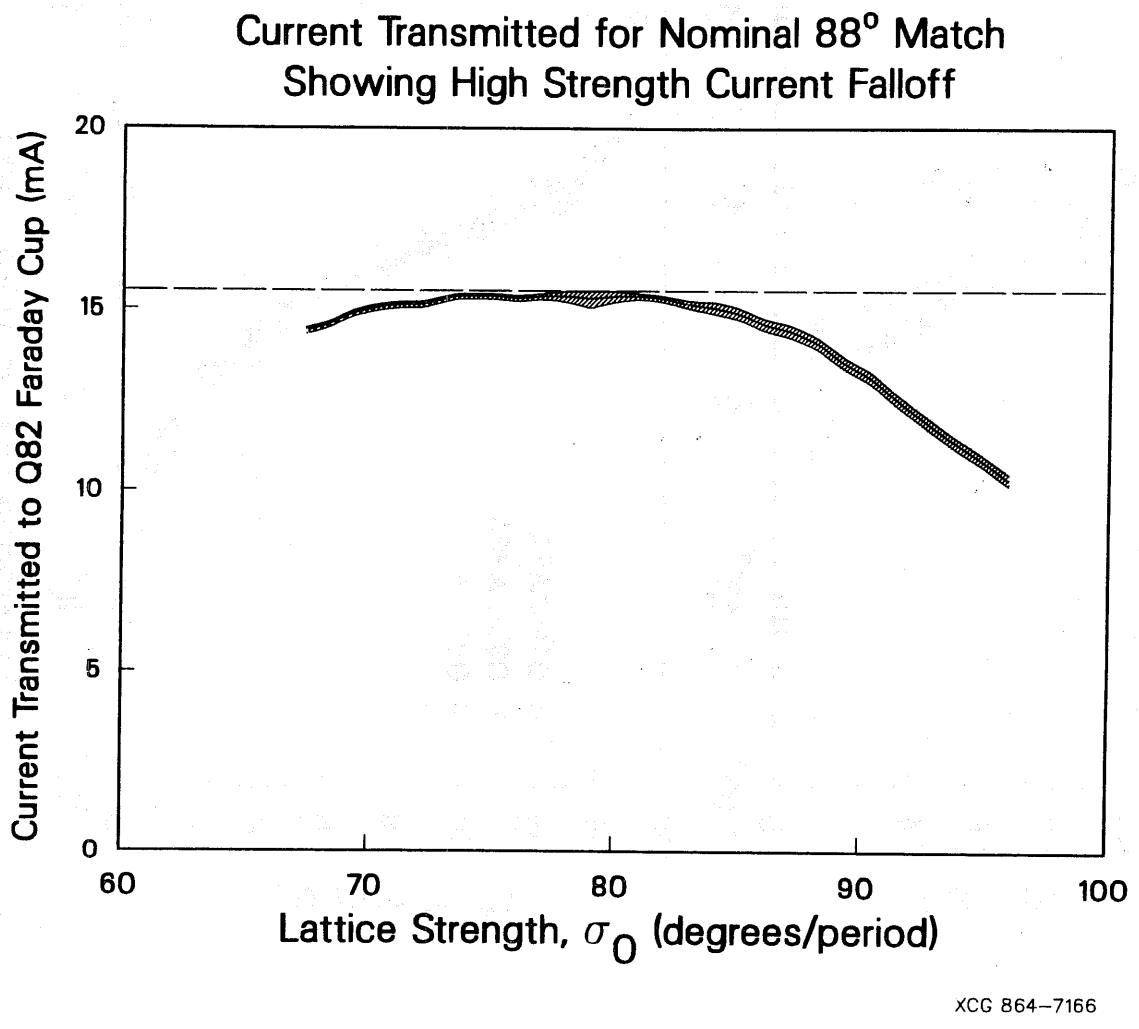

Figure 5.9: Current transmitted through the lattice for $\sigma_0 \sim 90°$, showing the falloff in transmitted current for $\sigma_0 \sim 90°$. The beam loss at the low lattice strength end of the plot is due to mismatch of the beam.

are characterized by perturbed electrostatic potential functions expressible in terms of finite polynomials in x and y [15,16]. The various modes were classified by the order of the polynomials. (For example, for a "third-order" mode, the highest-order term in the perturbed potential is x^2y or y^3.)

In addition, there is the possiblity that in a beam with a high degree of order, such as a K-V distribution, negative-energy modes of oscillation can exist and become degenerate in frequency with positive energy modes. The resulting energy transfer between modes can result in emittance degradation, in a way analogous to the two-stream instability in plasmas [17].

As a result of such calculations, there had been concern that the existence of $n = 3$ ("third-order") modes could require that σ_0 be limited to no greater than 60°, and that the threshold values of σ/σ_0 for fourth- and higher-order mode instability (about 0.4) would limit the space-charge depressed phase advance for $\sigma_0 = 60°$ to $\sigma = 24°$ [20].

Our work shows no evidence of any unstable behavior for the lowest accessible values of σ for lattice strength up to about $\sigma_0 = 88°$. There has, however, been some work on the limiting effects caused by interaction with induced charge on the lattice [41]. This effect may prove to be the practical limit on low-emittance beam transport. Our relevant measurements are discussed in section 6.2.

5.2.2 Plasma-like behavior

In the low-σ_0 limit, an alternating gradient lattice may be represented by a smooth-focusing equivalent for the purpose of calculating certain parameters of the beam. The smooth focusing model is physically equivalent to a fixed uniform background charge density of the opposite sign to that of the beam particles, and so the beam looks very much like a plasma. In this model, the K-V beam, as well as a Maxwellian beam for low transverse temperature, has

a circular cross-section and a uniform particle density. The projection of this distribution onto one spatial dimension gives a locus of current vs. x which is elliptical. Maxwellian solutions with a non-zero beam temperature have tails in the distribution in real space, with a scale length given by the Debye length appropriate to the density and transverse velocity spread of the beam. Within the plasma framework, the physical interpretation is simple. For a cold beam, the restoring well is almost neutralized by the beam particles over the bulk of the beam cross section, and the residual focusing field inside the beam is very small. The beam edge occurs at the location where the restoring well potential becomes comparable to the thermal energy of the particles. The beam density drops nearly to zero over a distance of about $2\lambda_D$. For cold beams, the particle density is nearly constant until this sheath is reached. The result is an elliptical 1-d current profile over the bulk of the beam, with small tails at the edges provided by the sheath particles.

We show in Fig. 5.10 a comparison between some of our measured beam profiles for $\sigma_0 = 59°$ near the end of the channel and smooth-focusing solutions calculated for Maxwellian distributions with the same current and RMS emittances as measured for the real beams. We take the distributions to be of the form

$$f_M(x,y) = n_0 \exp\left(-\frac{\kappa(x^2+y^2) - e\phi(x,y)}{kT}\right), \tag{5.1}$$

where κ is an effective spring constant for the lattice, $\phi(x,y)$ is the beam self-potential, and kT is the transverse temperature of the beam, in joules. We numerically integrated solutions to the Poisson equation, assuming a Maxwellian particle distribution. The physical extent of the tails in Fig. 5.10 is in reasonable agreement with the calculated value. The beam temperature,

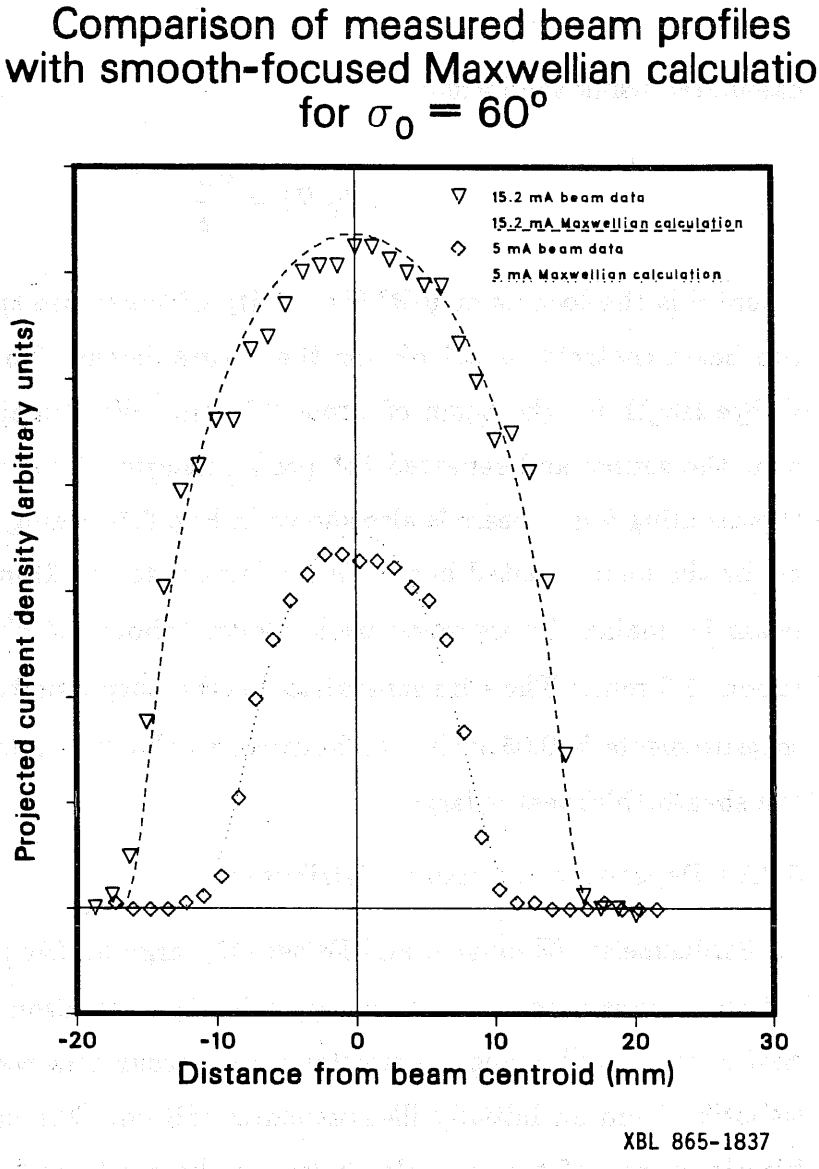

Figure 5.10: Transverse density distribution in x (measured by a traversing slit) for the 15-mA beam, and for a 5-mA beam, both for $\sigma_0 = 59°$. The dotted lines represent calculated profiles for Maxwellian transverse beam distributions in a smooth-focusing lattice. Small tails in real space due to the thermal tails of the distributions are visible. The calculated Debye length is about 0.7 mm ($kT/e \sim 2.3$ eV) for the 15-mA beam and 1.2 mm ($kT/e \sim 6.4$ eV) for the 5-mA beam.

calculated using the formula

$$T(\mathrm{eV}) = \frac{m\tilde{v}^2}{e}, \tag{5.2}$$

where $\tilde{v}$ is the local x or y RMS velocity of the phase space distribution at the beam centroid, is 2.3 eV for the 15-mA beam. This corresponds to a Debye length for the beam of about 0.7 mm. We also attenuated the beam near the source and repeated the profile measurement. The calculation for the resulting 5-mA beam is also shown in Fig. 5.10, using the same emittance as for the unattenuated beam. With respect to the 15-mA beam, the 5-ma beam is smaller, its temperature is higher (about 6.4 eV), and λ_D is larger (about 1.2 mm). The wire separation for the harp monitor used to make the measurements is 0.05 inches (1.25 mm), so that the relative uncertainty in the sheath thickness is large.

5.2.3 Dependence on source distribution

Strückmeier, Klabunde, and Reiser [42], arguing from the general conservation of transverse energy, and supported by simulation results, have shown that a very rapid change in emittance can occur as a result of charge redistribution from an initially ill-matched condition. The change in transverse kinetic energy of the particles balances the electrostatic energy change of the beam. These ideas have been developed further by Wangler [43] and Anderson [44].

In these works, it has been shown that in the low-σ limit, with linear external focusing, the beam will distribute its space charge approximately uniformly in configuration space. If the source provides a distribution of current that is too strongly peaked toward the axis, the charge will subsequently spread out as the distribution relaxes. The initial electrostatic energy

is higher than the final, and the difference shows up in the random transverse energy of the beam, causing the emittance to rise. An inverse situation can occur for initially hollow beam distributions.

While we have seen no collective increase in emittance for $\sigma_0 < 88°$, there have been results from Klabunde [23] at GSI in Darmstadt, Germany, indicating that for $\sigma_0 = 60°$, and an initial beam current and emittance corresponding to our lowest emittance conditions ($\sigma \sim 7°$), but with an initially Gaussian distribution of charge in configuration space, the beam emittance grows significantly within the first few periods of transport, a distance short compared to a plasma period. It is probable that this effect is due to the non-uniform initial beam distribution, as described above. The GSI results are somewhat clouded, however, in that the lattice is magnetic, and the experiments are made using a long-pulse plasma source, which results in significant background gas neutralization as the pulse progresses. To extract data without neutralization perturbations, they use measurements only early in the pulse.

For the SBTE, we have no recent measurements of the source emittance to compare with that measured after Q4. However, as mentioned in section 5.1.1, the SBTE source produces a relatively uniform current density (see Fig. 5.1), so that this rapid increase in emittance should have little driving energy. In addition, our early measurements of emittance (using the original aluminosilicate coatings) gave about the same value as later measurements downstream.

5.3 Results for $\sigma_0 \geq 88°$

It was expected that the regime of lattice strength $\sigma_0 \geq 90°$ would be unsuitable for intense beam transport, because of instability in the envelope equations [20,40]. Nonetheless, in this thesis investigation we explored this

region of parameter space and discovered behavior which to date has no satisfactory theoretical description (a semi-empirical conjectured description will be discussed later, in sec. 5.5).

The analytical work on the stability of the envelope equations is directly relevant for non-K-V beams. Because the K-V and RMS envelope equations are identical in form, they have the same stability properties. Instability in RMS radius will result in a large portion of the beam attaining a large displacement within the bore, with subsequent beam loss. The regions of envelope stability and instability are included in Fig. 5.11, along with the final results of our beam measurements in terms of stable limiting values of σ and σ_0.

We found no evidence of collective beam interaction for $\sigma_0 \leq 83°$. At $\sigma_0 = 88°$, a small beam loss occurred, with no effect on the beam emittance. This marks the first onset of collective beam effects in the course of our measurements. In contrast, for $\sigma_0 > 90°$, the unattenuated beam from our source is violently unstable, and we must greatly decrease the contribution of space-charge forces with respect to the emittance in order to ensure stability. To aid in determining the high-σ_0 stability boundary, we installed a three-grid emittance spoiler in place of the single parallel-wire grid terminating the injector. The new grid assembly attenuated the beam current to 10.3 mA, because of the greater number of less transparent grids in the beam path. Because the first of the grids was coarser in structure (a hexagonal grid of 0.125-inch cell size) than the 0.05-inch spacing parallel-wire grid we had had in place, the output emittance rose to about 2×10^{-7} π meter radian from the former 1.4×10^{-7} π meter radian, even with no external bias applied to the grids. (See Appendix C for the dependence of the emittance on the grid geometry.)

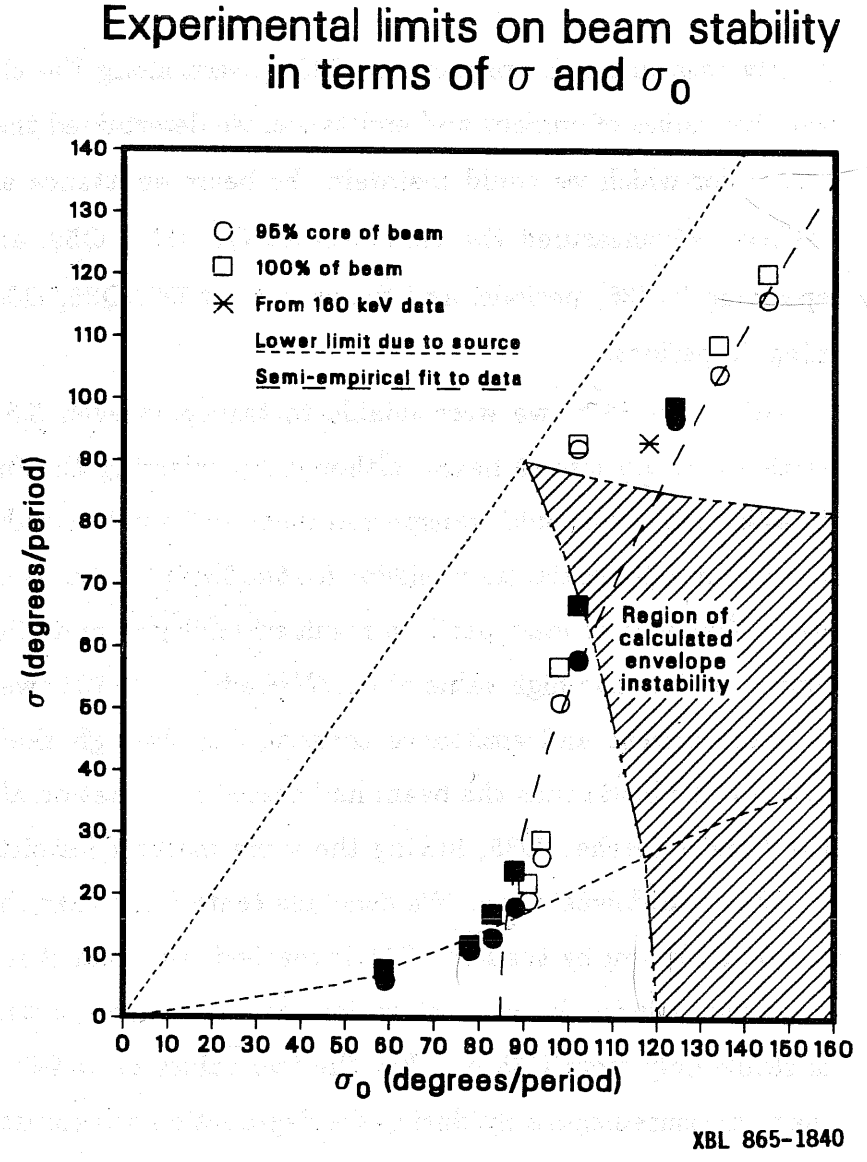

Figure 5.11: Summary of results for empirical stability of beams in A.G. lattice. The shaded region marks the area of instability of the envelope equations. For $\sigma_0 < 88°$, the data are limited by the emittance of the SBTE source. For $\sigma_0 > 88°$, the points mark the empirical collective stability boundary. The solid symbols mark beam parameters for which the current and emittance were conserved throughout the SBTE. We have also plotted results for which the beam stabilized during transport through the channel, as discussed in the text for the various cases. The hyperbola plotted with the data is described in section 5.5.

By measuring the properties of the beam along the channel for various relative values of current and emittance, we determined the minimum values of ϵ/I for which we could maintain the beam emittance and current in the lattice. We measured the emittance at Q4, Q35, Q59, and Q80 (or Q76), spanning 38 (36) periods, and the current at Q2, Q36, Q60, and Q82, spanning 40 periods.

For $\sigma_0 > 130°$, we were unable to transport even 3.5 mA through the lattice with no loss of beam, although by injecting the full 10.3 mA beam into the lattice we could transport as much as 7.4 mA to the DFC at Q82. The reason for only partial transmission for the 3.5 mA beam is not known, though we believe it is at least partly a result of matching and alignment problems, aggravated by the high value of σ_0. While for $\sigma_0 > 124°$ we had no examples of total current and emittance conservation through the SBTE lattice, in some of the beam runs the beam had ceased its variation along the lattice by the time it reached Q35, having the same measured emittance and current for Q35 and downstream. We conclude tentatively that the beam reaches a new equilibrium by the time Q35 is reached, and that it is stable thereafter. We have included in our results data for these cases, noting that the beam is stable only from Q35 on. For the two values $\sigma_0 = 94°$ and $\sigma_0 = 98°$, we made measurements only during the degradation of an unstable beam, but in these instances, the beam distribution remained constant between Q59 and Q80. For these two cases, as well, we have plotted the output parameters in Fig. 5.11. More information about these beam measurements is included in section 5.3.2.

5.3.1 Envelope measurements

We have compared the measured RMS radius of the beam with that calculated from σ_0 and the measured current and emittance, using the envelope

equations, in the last two columns of Table 5.1. The measured radius will vary along the lattice from the average value because of imperfect matching, but the resulting oscillations have been observed at low σ_0 to damp considerably through the channel, as shown in Fig. 5.4 for $\sigma_0 = 59°$ and $\sigma_0 = 83°$.

5.3.2 Phase space measurement results

We have calculated from solutions to the envelope equations the corresponding values of σ for a K-V model beam with the same current and RMS emittance as measured for the real beam. Those values have been entered into Table 5.1 and plotted in Fig. 5.11. An analysis of these data has been published previously by Tiefenback and Keefe [25], but using values of beam energy 2% too low (caused by an error in time-of-flight measurements with a high-current beam). This calibration error resulted in quoted values for the paraxial σ_0 that were too high by about 1° for $\sigma_0 \sim 60°$, 2° for $\sigma_0 \sim 90°$, and 5° for $\sigma_0 \sim 150°$. Results quoted by Tiefenback and Keefe for the range $60° \leq \sigma_0 \leq 150°$ actually span the range $59° \leq \sigma_0 \leq 145°$ for paraxial particles. See section 7.1 for more information on errors in σ_0.

In the following figures, Figs. 5.12–5.25, we show the results of measurements made over the range $88° \leq \sigma_0 \leq 145°$. The letters "H" and "V" in the legends for the i vs. $\epsilon(i)$ plots denote measurements made in the horizontal and vertical dimensions, respectively. The contour levels in the phase space data are chosen to lie at levels containing approximately 50%, 60%, 70%, 80%, 90%, and 95% of the beam. Thus the contours do not surround a region of constant current, at least in the case of unstable beams for which the current varies along the channel. An additional complication is that the two transverse dimensions are not completely independent, as they would be in the case of negligible self-field for linear focusing . The 4-d nature of the phase space allows variations in the contours not expected for purely 2-d

σ_0	I_{out}	i/I	$\epsilon(i)$	$\sigma(i)$	$2\tilde{x}$	R_0
59°	15.2	1.00	1.38	8.°	15.7	15.3
		0.95	0.97	6.°	15.5	14.9
78°	15.2	1.00	1.32	12.°	12.3	12.1
		0.95	1.08	11.°	12.0	11.8
83°	15.2	1.00	1.6	17.°	12.5	11.6
		0.95	1.15	13.°	12.2	11.2
88°	14.3 of	1.00	2.00	24.°	11.6	11.0
	15.2 inj.	0.95	1.45	18.°	11.2	10.5
91°	13.0 of	1.00	1.54	22.°	10.3	10.1
	15.2 inj.	0.95	1.26	19.°	9.9	9.8
95°	10.6 of	1.00	1.68	29.°	9.5	9.1
	15.2 inj.	0.95	1.38	26.°	8.8	8.8
98°	8.5 of	1.00	3.33	57.°	9.4	9.3
	10.3 inj.	0.95	2.56	51.°	8.9	8.6
102°	5.4	1.00	2.65	67.°	7.2	7.8
		0.95	1.85	58.°	6.5	6.9
102°	5.3 of	1.00	8.8	93.°	12.8	12.5
	5.4	0.95	7.9	92.°	12.2	11.9
118°	3.45	1.00	2.16	93.°	6.6	5.9
(160 keV)		0.95	—	—	—	—
124°	5.4	1.00	4.00	99.°	8.2	8.6
		0.95	3.5	97.°	7.6	8.1
134°	2.7 of	1.00	2.06	108.°	6.2	6.2
	3.4 inj.	0.95	1.67	103.°	5.6	5.6
134°	5.0 of	1.00	3.9	110.°	8.2	8.5
	10.3 inj.	0.95	3.2	105.°	7.8	7.8
145°	2.5 of	1.00	2.7	125.°	6.9	7.2
	3.4 inj.	0.95	2.2	121.°	6.4	6.5
145°	4.6 of	1.00	3.4	116.°	7.8	8.1
	10.3 inj.	0.95	2.8	111.°	7.2	7.3

Table 5.1: Comparison between calculated and measured beam envelope radius, including current, emittance, and derived σ values. Values for σ and σ_0 are in degrees/period, current in mA, emittance in $10^{-7}\pi$ meter radian, and radius values in mm. The value R_0 calculated from the envelope equations is for the midplane between quadrupoles.

evolution (see section 6.1). The plots all cover the same area in phase space, and are drawn to the same scale, covering about ±35 milliradians in angle and ±20 mm in position. The vertical scales for the perspective views are also the same (with one exception in Fig. 5.23), except that no allowance has been made for the varying calibration of the detectors (from such effects as variation of the width of the collimating slits at the various measurement stations). All are centered on the beam centroid, which is near the beam-line axis except for very high σ_0, for which the lens misalignment becomes important over the length of the channel. In some of the contour plots, the position axis was lost in the figure preparation, but in most of these cases, the corresponding perspective view (from the upper right-hand corner of the contour map) is shown with the same axes, fully labeled. The perspective views are included to aid interpretation of the contour maps.

The onset of instability may be seen at $\sigma_0 = 88°$ with the full 15 mA beam current of the SBTE with minimum emittance. The results of our measurements are shown in Figs. 5.12 and 5.13. There is a small beam loss through the SBTE for these parameters, about 4–5%, although the emittance is constant. The only significant change in the phase space distribution of the beam is a rearrangement of the perturbed portions of the beam visible in the Q4 contour map in Fig. 5.13. This is the same phenomenon shown in Fig. 5.2. The beam remains unchanged between Q59 and Q80. The Q4 RMS curve in Fig. 5.12 is steeper than the curves from the other measurement positions. This is a result of the RMS calculation, which weights particles far from the phase space centroid more heavily than those near the centroid. The shape of the beam contour, and not just the area in phase space occupied by the contour, influences the RMS emittance calculation.

In Figs. 5.14 and 5.15, we show the results of injecting a 10-mA beam

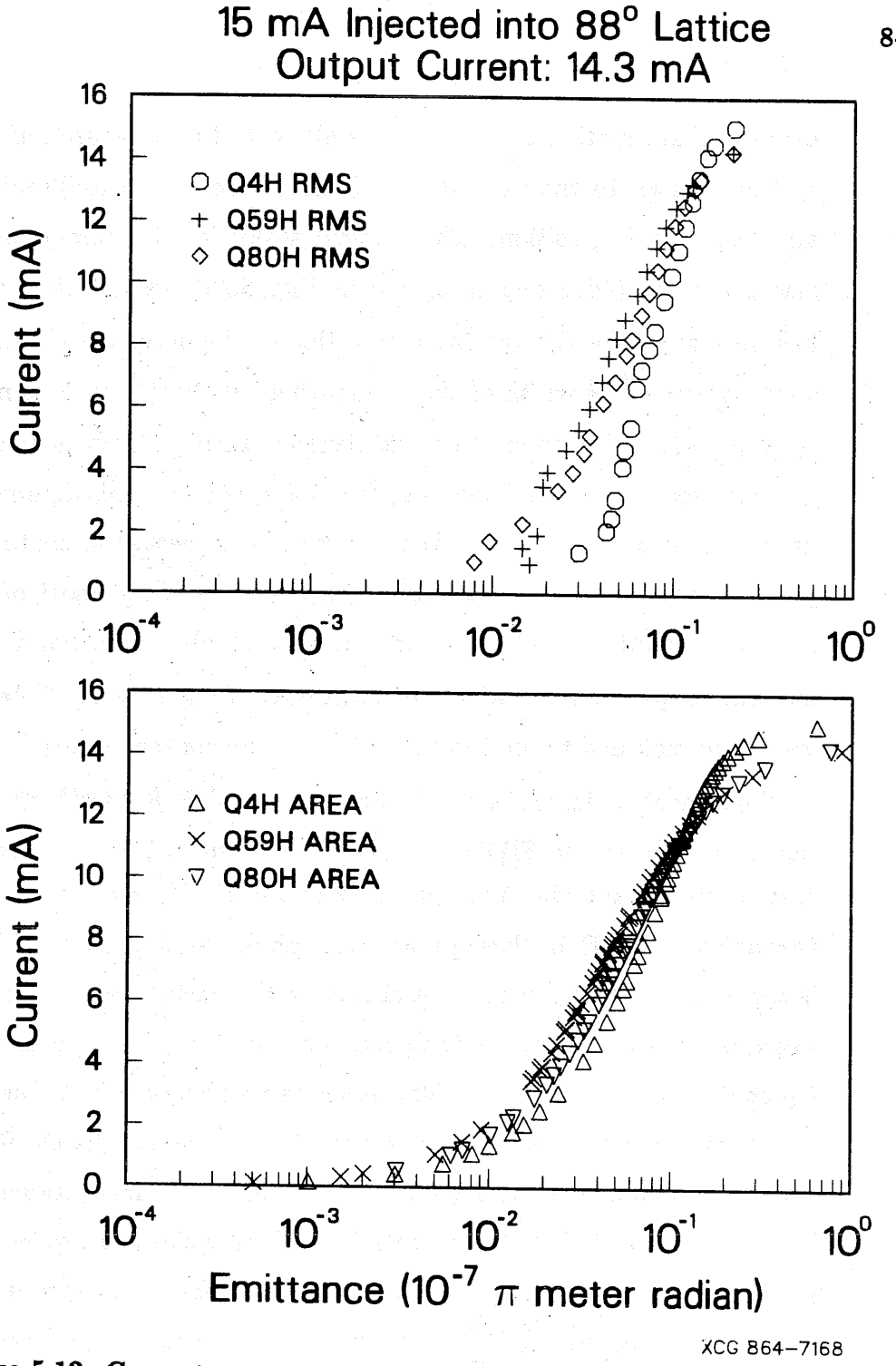

Figure 5.12: Current vs. emittance for $\sigma_0 = 88°$. The Q4 RMS curve shows a higher emittance for fractional beam current because of the distortion in its phase space distribution, compared to Q59 and Q80. The distributions at Q59 and Q80, however, are very similar.

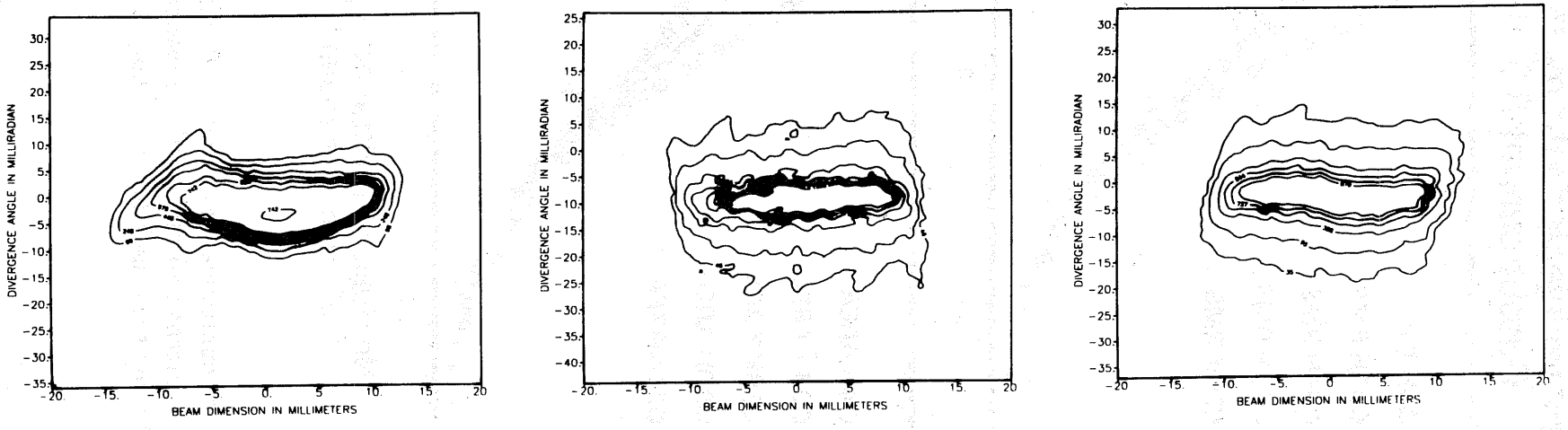

XBL 865-1873

Figure 5.13: Phase space contours for $\sigma_0 = 88°$. The phase space distribution at Q4 appears not too severely aberrated. At a lower level than is shown in the contour map, however, there is an arm-like structure, parallel to the flat left end of the outermost contour, pointing to the upper right. This structure does not persist in measurements further along the lattice. The low-level contours (containing 90% or more of the beam), become greater in extent as the beam propagates along the channel, but the beam shows no change between Q59 and Q80.

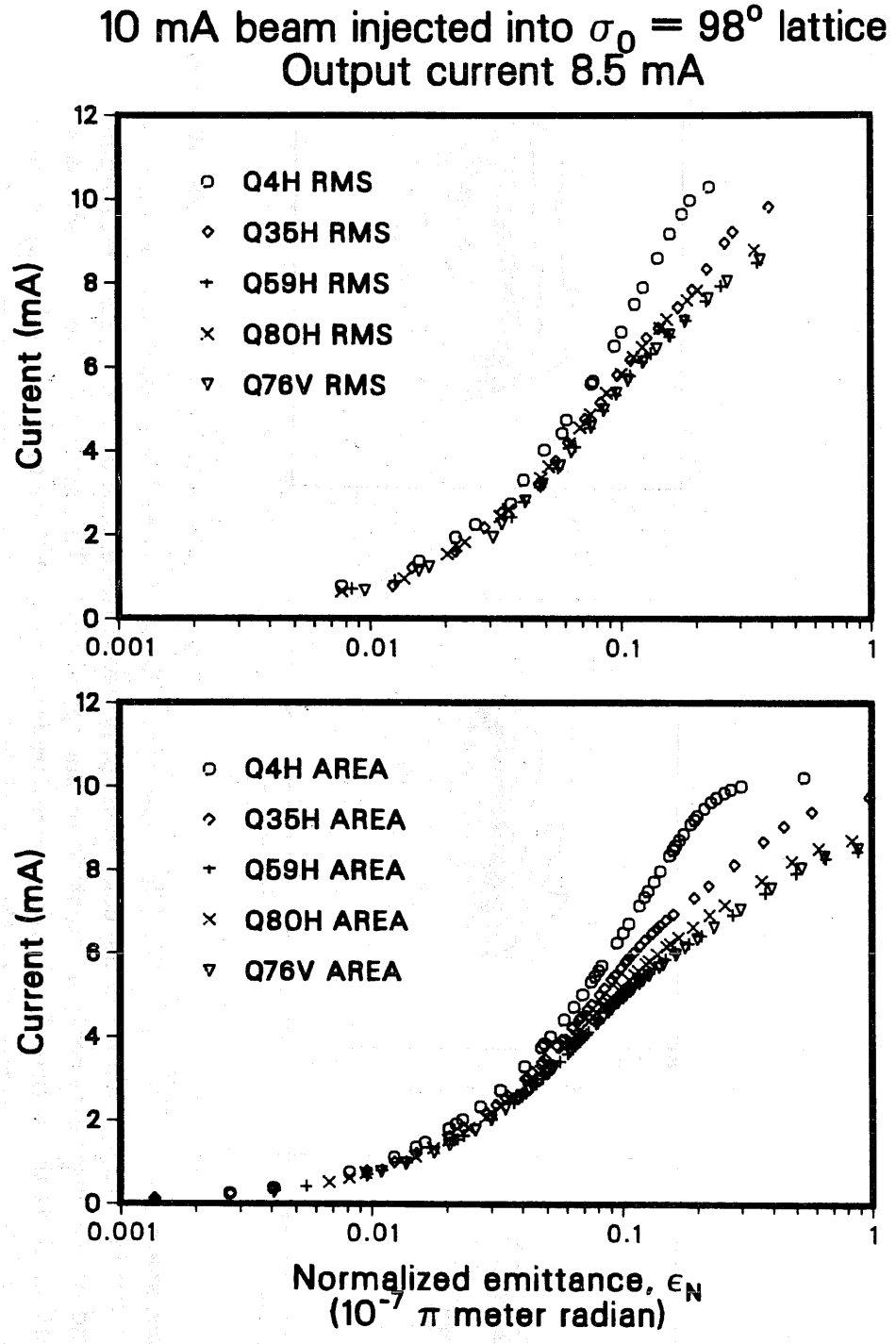

XBL 865-1891

Figure 5.14: Current vs. emittance for $\sigma_0 = 98°$. The instability of the beam shows up in decreased current and increased emittance. The curves for Q59 and for Q76 and Q80 show that the beam is no longer changing downstream of Q59.

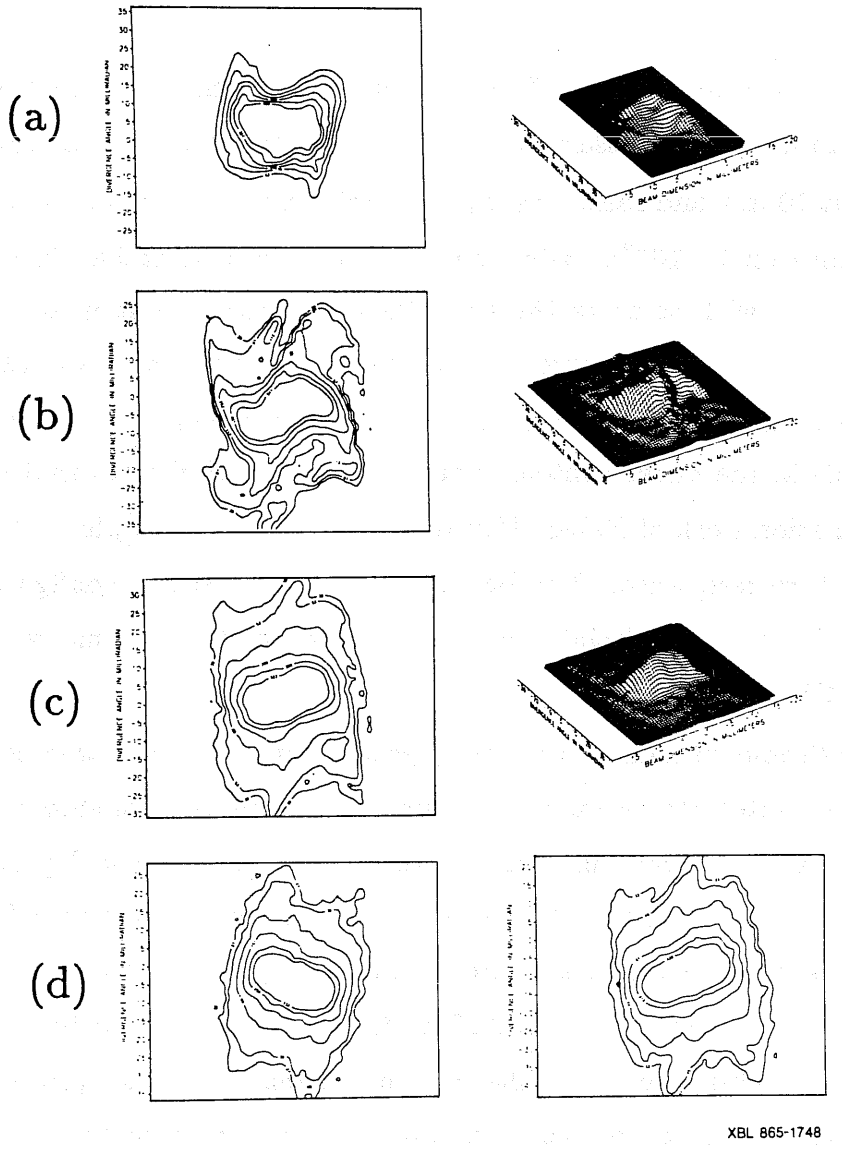

Figure 5.15: Phase space contours for $\sigma_0 = 98°$. The perspective views are for the contour maps at the left for Q4 in row (a), Q35 in row (b), and Q59 in row (b). In row (d) are contour maps for Q80 (horizontal) on the left and Q76 (vertical) on the right. The evolution of the beam between Q4 and Q35 shows a four-pointed structure which is apparent in our other measurements only for $\sigma_0 = 102°$. The structure is similar to that shown in some simulation work by Haber and Maschke [45] and by Hofmann [46] for strongly focused beams. As the beam propagates downstream, the structure becomes much less prominent, and the beam ultimately stabilizes.

into a $\sigma_0 = 98°$ lattice. The injector grid had been replaced by the 3-grid emittance control assembly, which attenuates the beam at the injector to about 10 mA and raises the injector emittance from about $1.4 \times 10^{-7}\pi$ meter radian to $2.0 \times 10^{-7}\pi$ meter radian. The beam is unstable even at this lower intensity, with some of the particles being pushed out in phase space and lost to the channel electrodes. The beam current stabilizes at about 8.5 mA, with an emittance of about $2.6 \times 10^{-7}\pi$ meter radian. There is some structure visible in the phase contour plots in Fig. 5.14, similar to that shown in the simulation work of Haber, Hofmann, and others [45,46], for a "fourth order" structure resonance. The beam has reached a stable configuration by the time it has reached Q59, however, showing no further change between Q59 and Q80.

Without revising the matching section lens strengths, we raised σ_0 to 102° and repeated the beam measurements. The results are shown in Figs. 5.16 and 5.17. The contour plots are very similar to those of Fig. 5.15, although the beam does not completely come to a stable configuration before it reaches Q59, evolving somewhat more on the way to Q76. The contour map and perspective view for $\sigma_0 = 102°$ at Q76 are very similar to those for $\sigma_0 = 98°$. We also attenuated the injector current to 5.4 mA, and after careful adjustment of the matching section, we were able to transport the entire current through the SBTE, with an output emittance of about $(1.9 \pm 0.1) \times 10^{-7}\pi$ meter radian, compared to the $2.0 \times 10^{-7}\pi$ meter radian injection emittance value. These are the parameters used for the lower set of points for $\sigma_0 = 102°$ in Fig. 5.11.

We were unable for some time to transport the 5.4-mA beam through the lattice for $\sigma_0 = 102°$. It is clear in Fig. 5.11 that these beam parameters place the beam very near the high-intensity (low-emittance) boundary of

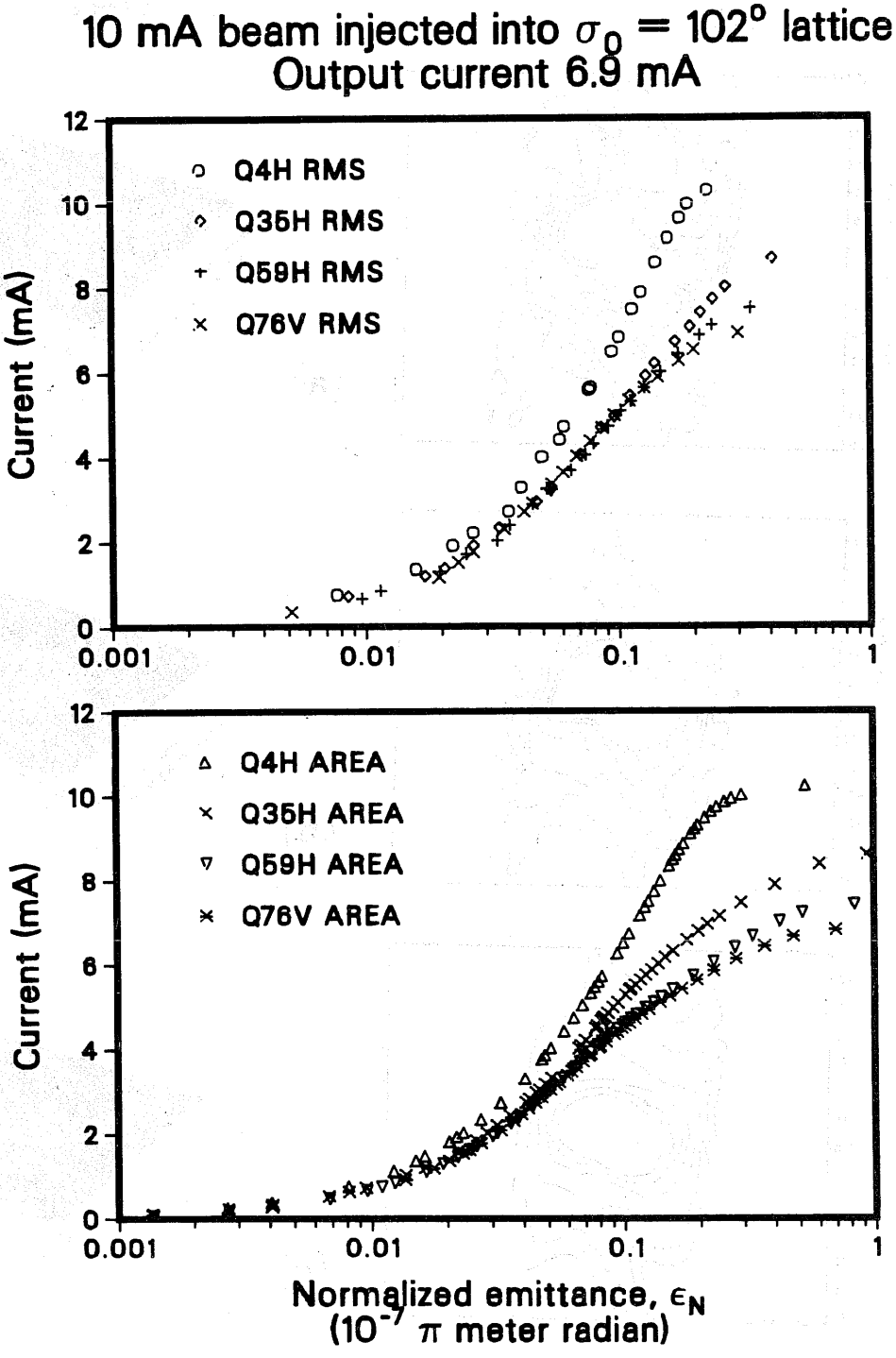

XBL 865-1890

Figure 5.16: Current vs. emittance for $\sigma_0 = 102°$. The major change occurs between Q4 and Q35 for the RMS curves, with the evolution nearly complete by the arrival of the beam at Q59. The current measured on the Q60 SFC is 7.2 mA, and the current at Q82 is 6.9 mA. The area emittance continues to rise even as more current is lost on the way to Q59, but little more change occurs before Q76.

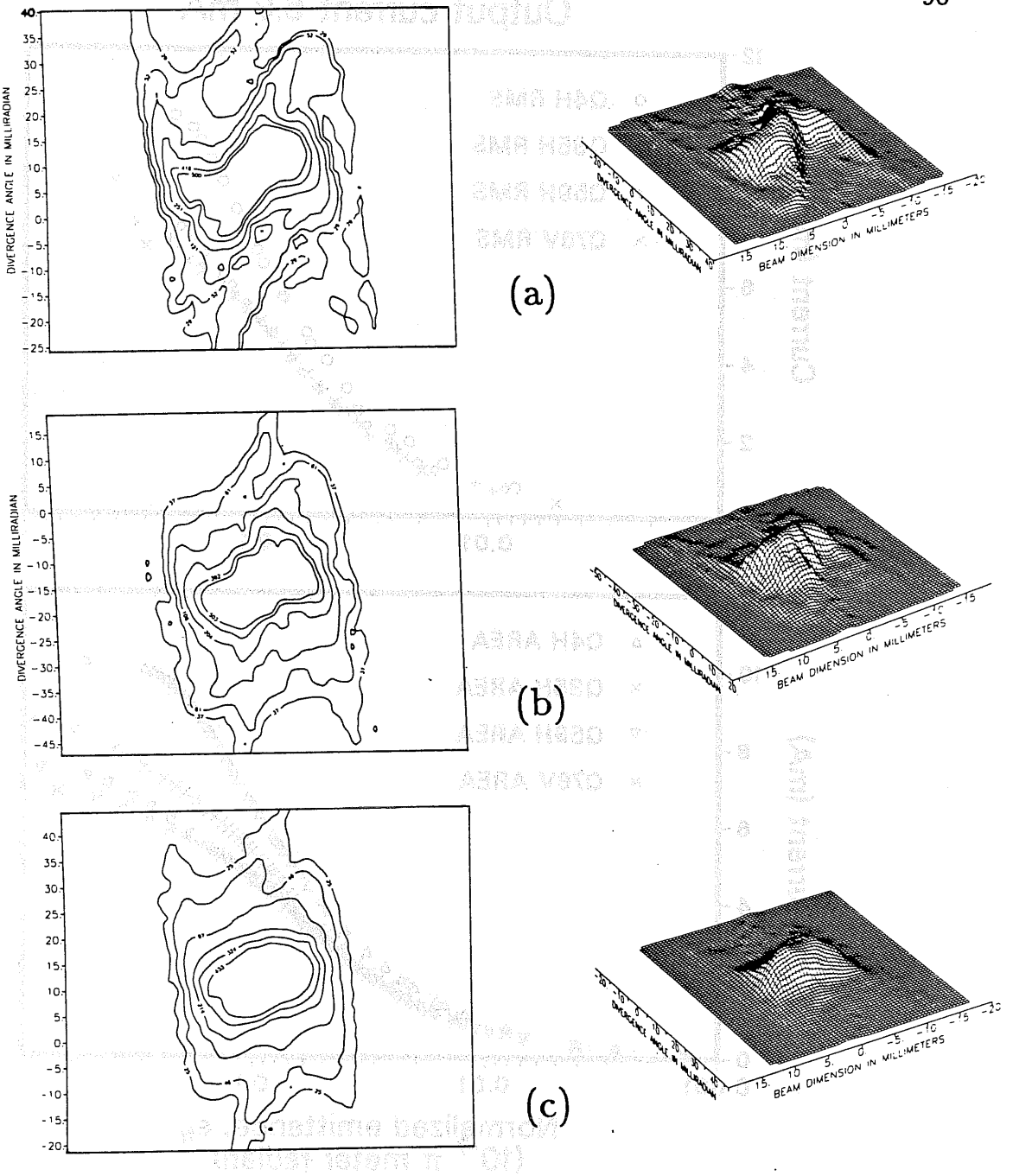

XBL 865-1747

Figure 5.17: Phase space contours for $\sigma_0 = 102°$. The perspective views correspond to the contour maps to the left of each for (a) Q35, (b) Q59, and (c) Q76. The four-pointed structure again is visible at Q35, and remains visible to some extent at Q59. The beam is very nearly stabilized by this point, evolving little in the remaining transport to Q76.

the envelope instability, and this is apparently the reason the difficulty in matching the beam into the lattice for transport to Q82 without attenuation. We also tried to use the emittance grids to raise the emittance, in an attempt to improve the current transmission, when we found that some of the beam was lost in the channel. This approach was successful for $\sigma_0 = 124°$, as shown below, but for this case, we could obtain a maximum current of 5.3 mA only by raising the bias on the grids to near the breakdown limit. We measured the beam emittance as far as Q59, obtaining values much higher than we expected at Q35 and Q59. The emittance we measured at Q4 with the emittance grid bias raised to 12 kV, was $5 \times 10^{-7}\pi$ meter radian, while the emittance measured at Q35 and Q59 was $8 \times 10^{-7}\pi$ meter radian, by far the highest value of the beam emittance that we have observed. The maximum beam size according to the envelope equations for this emittance is 20 mm, so this emittance is close to the acceptance of the SBTE for this value of σ_0.

We later recognized that the source of our difficulty was the envelope instability band, and we attribute the high emittance values measured at Q35 and Q59 to the effect of the instability. Because the current was approximately conserved throughout the channel and because the emittance of the beam was constant for Q35 and Q59, we have included the beam parameters for this case in Table 5.1 and Fig. 5.11. We thus have observed stable transport on either side of the envelope instability band for $\sigma_0 = 102°$. We were unable to maintain beam parameters for which the beam was within the envelope instability band.

We made our measurements for $\sigma_0 = 118°$ when we were operating at a particle energy of 160 keV. We used a beam current of 3.45 mA, and raised the normalized emittance from the minimum value of $1.2 \times 10^{-7}\pi$ meter radian for that injector configuration into the neighborhood of $2.2 \times 10^{-7}\pi$ meter radian, using the emittance spoiling grids discussed in Appendix C.

The results of this series of measurements are shown in Fig. 5.18. The error bars represent the estimated accuracy of ±10%, with a precision estimated from the reproducibility and systematic consistency of the measurements to be about ±5%. For these measurements, the current is constant at 3.45 mA along the channel (equivalent to 2.25 mA at 120 keV). Sufficient clearance was provided to accomodate the increased emittance of the beam in cases of instability. For low values of injection emittance, the output emittance increases by as much a as a factor of 2.5, and overshoots the value ultimately found to correspond to the stability threshold. As the injection emittance is raised, the output emittance falls until the two values meet. With further increases in the injection emittance, the output emittance increases proportionally.

At the time of these measurements, we had not installed the automated data acquisition system, and data logging and analysis were manual operations. To calculate the emittance of the beam, we scanned carefully across the beam with a single traversing slit to obtain the current profile, and calculated the RMS radius of the beam. We then selected several locations within the beam for scans of the distribution in transverse angle. We always found that the RMS angular width of the distribution was nearly constant across the beam (also noted in the higher-resolution measurements made later), although the amplitude of the distribution varies with the position in real space. In this feature, the beam is similar to a Maxwellian distribution, which has a constant "temperature" throughout the beam. In contrast, the K-V model beam, with its elliptical boundary enclosing a uniform density in phase space, has a local RMS angular width decreasing with distance from the beam center. We calculated the local RMS angle of the beam near the beam centroid, and took the emittance of the beam as four times the product of the RMS radius and angle, including the relativistic factor $\beta_r\gamma$ for the nor-

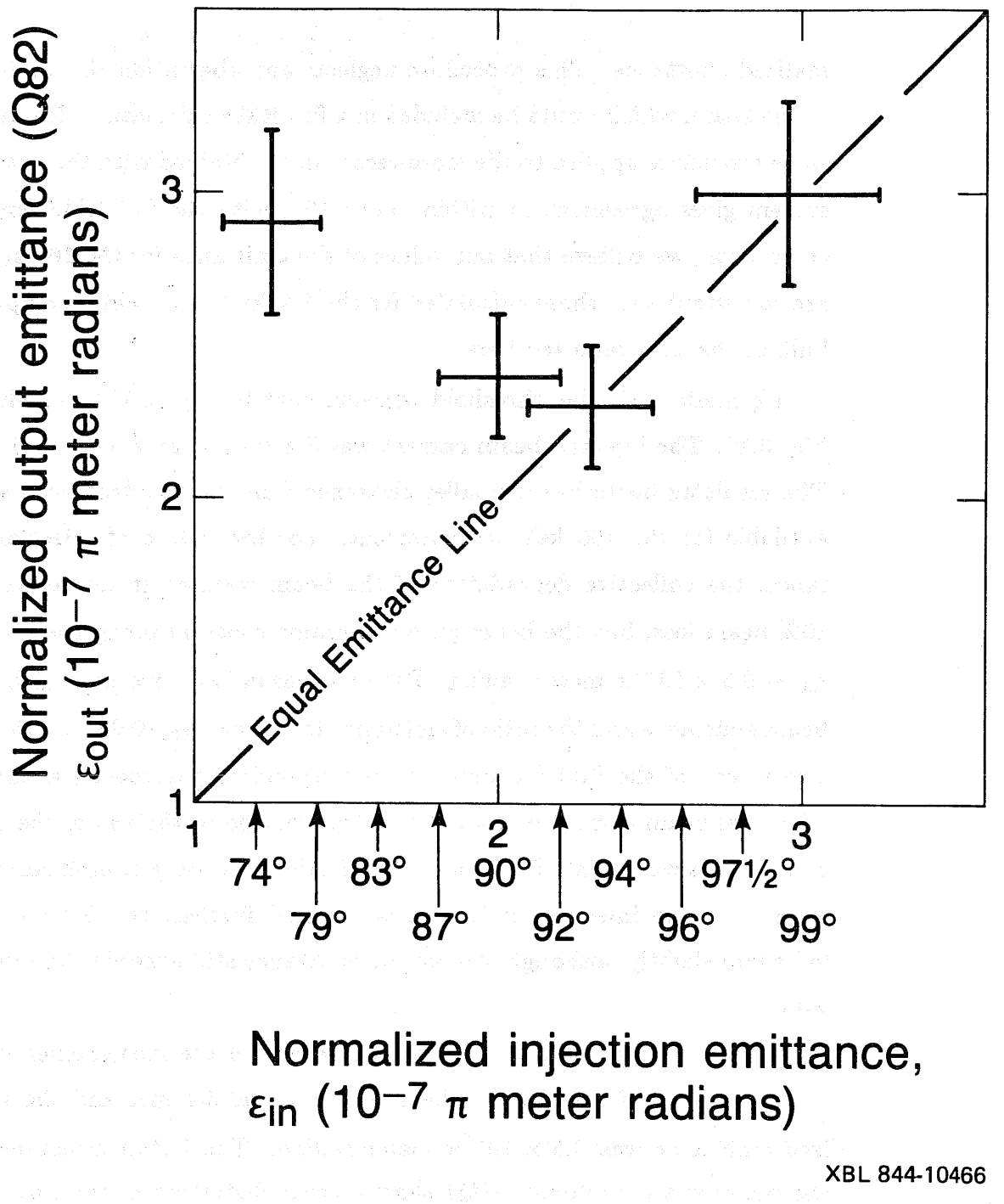

Figure 5.18: Threshold measurement for $\sigma_0 = 118°$. For the lowest plotted initial value of the emittance, the output emittance has grown by more than a factor of 2. As the injection emittance is raised, the output emittance falls, achieving equality at about $2.3 \times 10^{-7}\pi$ meter radian. For higher values of emittance at injection, the emittance at the output rises proportionally. The error bars plotted are based on a 10% estimate of overall accuracy.

malized emittance. This procedure neglects any aberrations in the focusing of the beam, which would be included in a full RMS calculation. Because this same procedure applied to the more-recent data obtained with the automated system gives agreement to within about 10% with the full RMS emittance calculation, we believe that our values of the emittance for the 160 keV runs are consistent with those calculated for the 120 keV runs, which comprise the bulk of the data reported here.

We made a similar threshold measurement for $\sigma_0 = 124°$, as shown in Fig. 5.19. The injected beam current was 5.4 mA, at an energy of 120 keV. The resulting beam has a smaller clearance from the quadrupoles than was available for the 160 keV measurement. For low values of injection emittance, the collective degradation of the beam resulted in approximately a 10% beam loss, but the beam current became constant along the lattice for $\epsilon_{95} \sim 3.5 \times 10^{-7}\pi$ meter radian. For this reason, we have plotted both the beam emittance and the ratio of emittance to current ($\epsilon_{95}/0.95I$) at the downstream end of the SBTE against the corresponding parameters at injection. The total beam current of 5.4 mA was transported to the end of the channel at the crossover point, for which the injection and output emittances were equal. As the injection emittance was raised further, the output current fell again slightly, although the output emittance still exceeded the injection value.

In Figs. 5.20 and 5.21, we show the results of the measurements at the crossover point, for which the beam current was 5.4 mA and the normalized emittance was $3.5 \times 10^{-7}\pi$ meter radian. The initial measurement of the phase space contours at Q4 show a great distortion of the phase space structure of the beam, with extensive gaps (relative to the peak density) in the distribution. These fill in as, presumably, the two transverse dimensions couple together to hide the voids in 4-dimensional phase space from detection

Variation of ϵ and ϵ/I at channel exit with values at injection

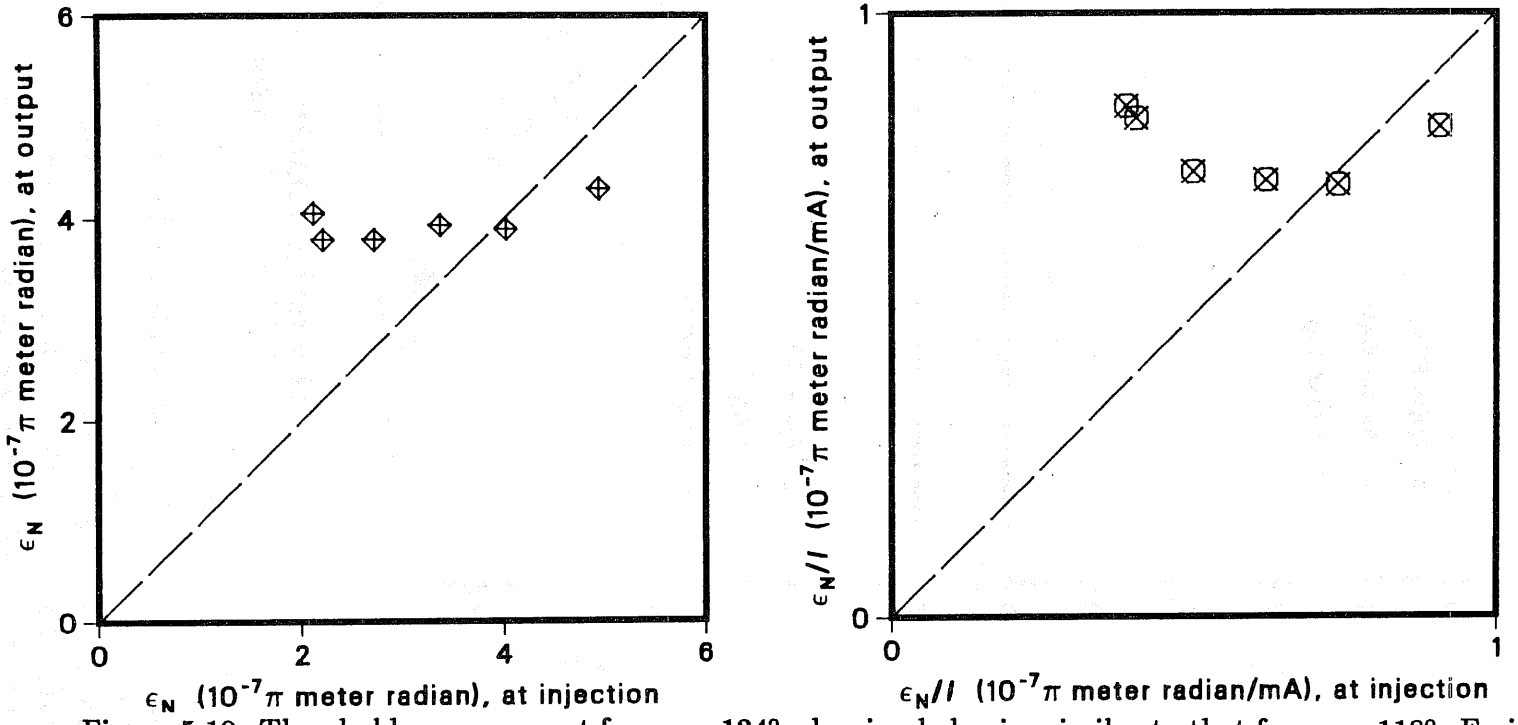

Figure 5.19: Threshold measurement for $\sigma_0 = 124°$, showing behavior similar to that for $\sigma_0 = 118°$. Emittance growth for unstable injection is accompanied by a small beam loss for the larger-diameter beam used here. The beam loss diminishes as the input emittance is increased, with the output emittance remaining nearly constant until the injection emittance rose above about $3.5 \times 10^{-7}\pi$ meter radian. The plot of ϵ_N/I at the end of the SBTE vs. the corresponding value at injection shows the same general features as for $\sigma_0 = 118°$. The total beam current is about 5.4 mA.

XBL 865-1844

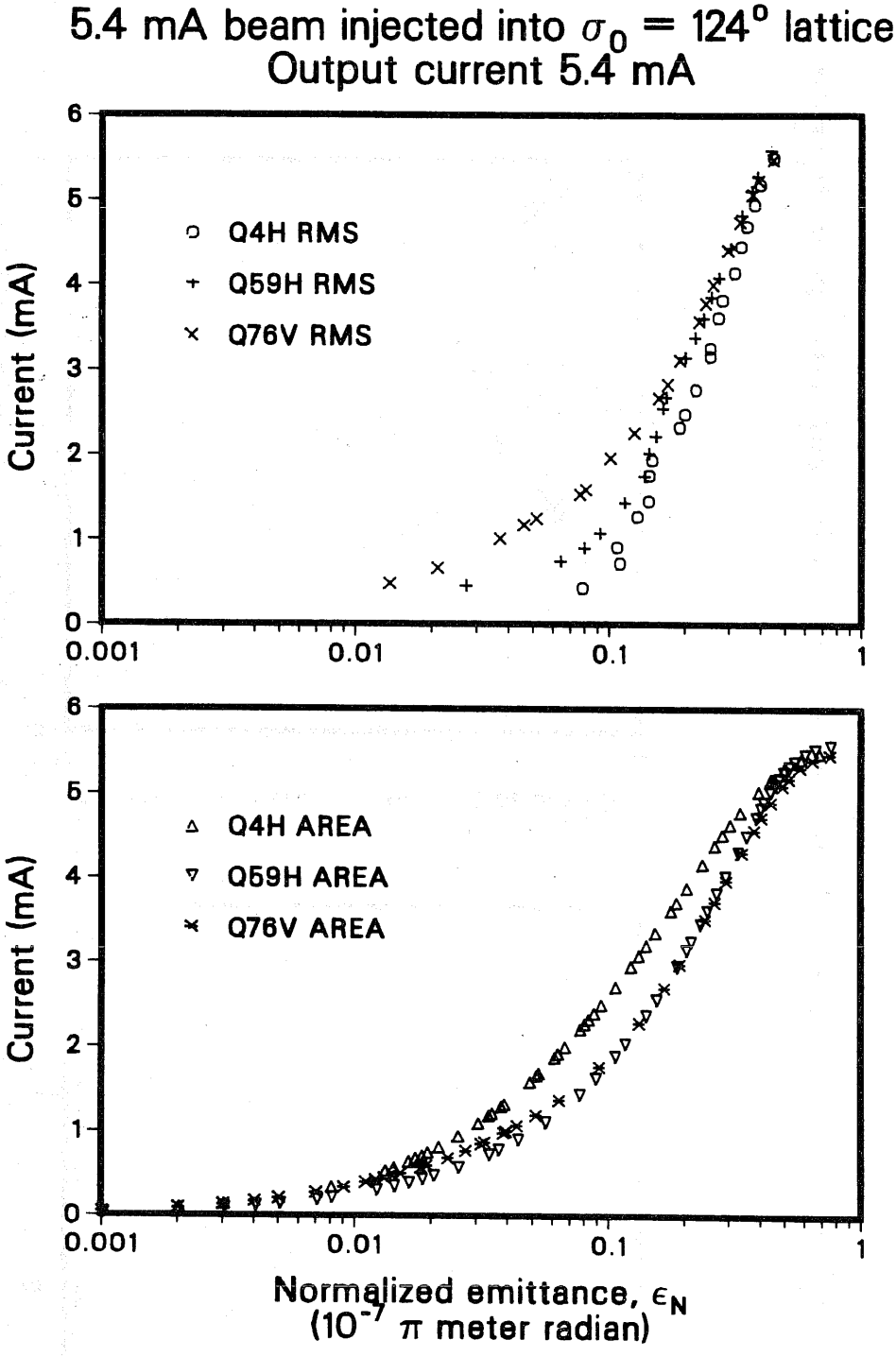

XBL 865-1889

Figure 5.20: Current vs. emittance for $\sigma_0 = 124°$. The behavior is similar to that of the previous examples, but the total emittance and current are constant throughout the lattice. The RMS emittance for the higher level partial beam distribution decreases, while for the area curves, the partial emittance increases between Q4 and Q59, becoming constant thereafter. The reason is clear from Fig. 5.21.

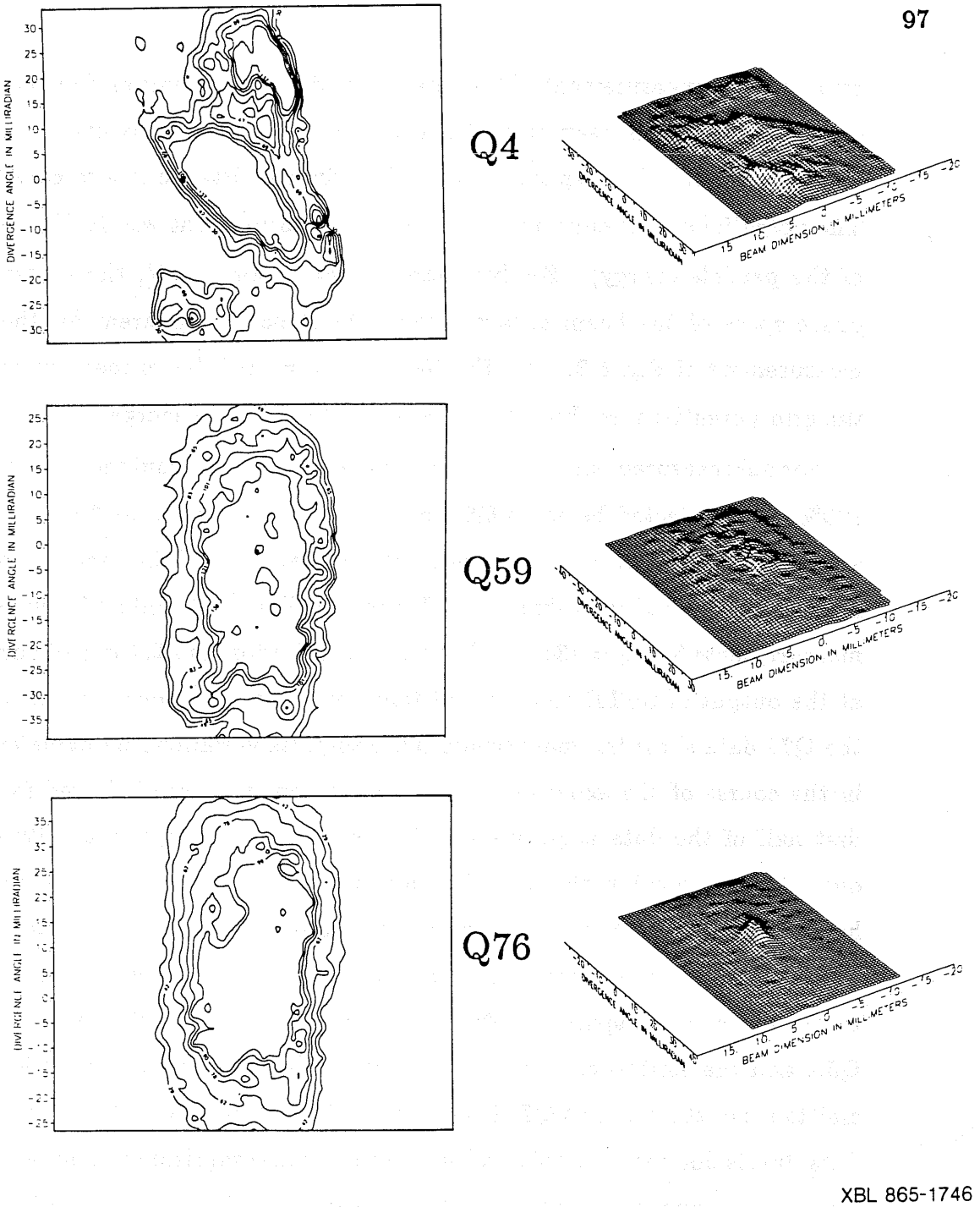

Figure 5.21: Phase space contours for $\sigma_0 = 124°$. The data are shown in rows for (top to bottom) Q4, Q59, and Q76. The distribution at Q4 is greatly altered by the emittance grids at the high bias (10 kV) in use. This structure was not present for the weaker bias potentials generally used, and it is not present in the downstream data. The dissipation of the structure introduced by the grids is the reason for the great increase in the partial area emittance curves shown in Fig. 5.20.

by a two-slit measurement. The total area of the distribution does not increase, although the beam particles distribute themselves more evenly in the two-dimensional phase space. The RMS-derived emittance is also constant. The potential on the emittance grids for this measurement was 10 kV ($\sim$ 8% of the particle energy). For bias values below about 6 kV, the transverse phase space of the beam does not show the structure apparent for the Q4 measurement of Fig. 5.21. For the 160 keV, $\sigma_0 = 118°$, beam measurements, the grid potential was about 6 kV ($\sim$ 4% of the particle energy).

For our measurements for $\sigma_0 = 134°$ and $\sigma_0 = 145°$, we could not transport 100% of the injected beam to Q82, even for currents as low as 3.4 mA. We attribute this at least in part to lens misalignments, which become markedly more important at high values of σ_0. We show in Figs. 5.22 and 5.23 a series of measurements for $\sigma_0 = 134°$, with 3.4 mA at injection and 2.7 mA of current at the output of SBTE and the emittance grids left grounded. In Fig. 5.23, the Q76 data show the most severe pulse-to-pulse variations we experienced in the course of the experiment. The experiment was well-behaved for the first half of the data acquisition period, giving poorer reproducibility over only the last portion the data for this run. There are only a few points having spurious high currents outside of the main body of the beam, and a few spurious zeroes inside the beam distribution. The overall outline of the beam in phase space at Q76 is very similar to the results for Q35 and Q59, and the emittances are also very close. The value we calculate for the emittance of the beam at Q76 is not sensitive to the positions of the spurious data, but is dominated by the well-behaved points comprising the body of the distribution, and we believe that the derived value of the emittance for Q76 is accurate. The emittance measured at Q35 was about $1.75 \times 10^{-7}\pi$ meter radian, which is less than the source emittance value of $2.0 \times 10^{-7}\pi$ meter

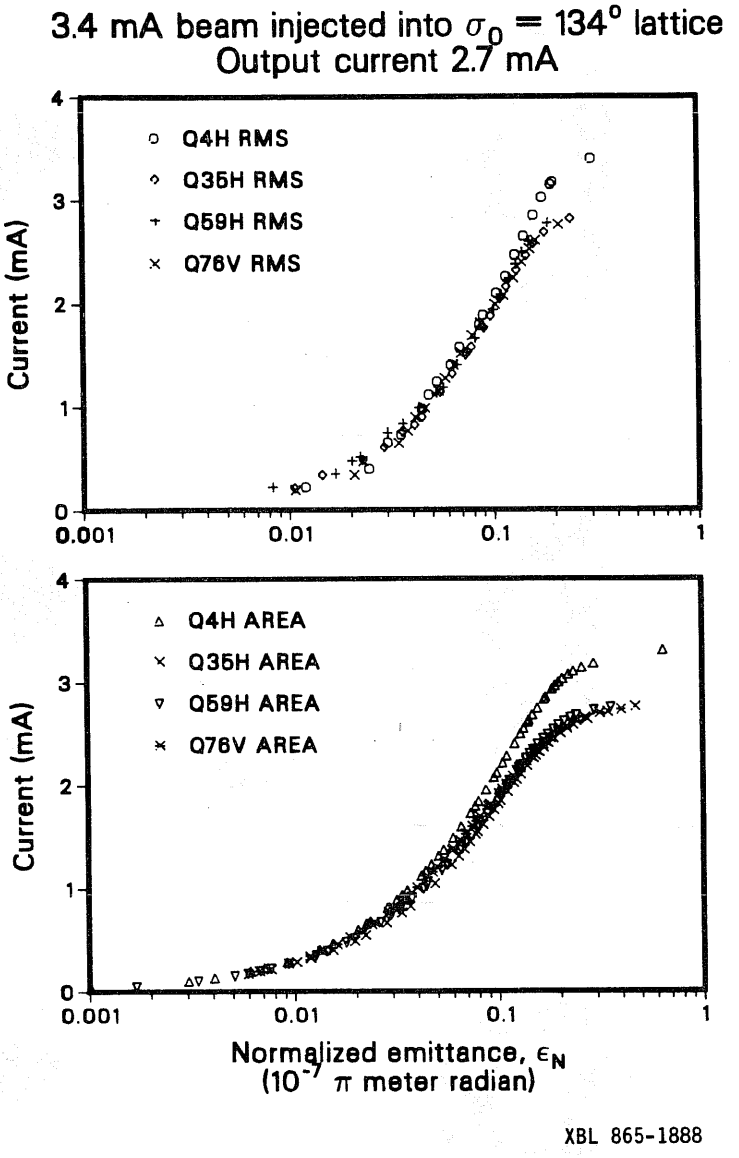

Figure 5.22: Current vs. emittance for $\sigma_0 = 134°$. The exact current in the beam for Q35 and Q59 is not certain, because of the absence of Faraday cup measurements. The current used for these plots is calculated by summing the data from the phase space measurements, using the cup-measured output current of 2.7 mA for the measurements at Q59 and Q76, for which the sum of the phase space points indicates, respectively, 2.6 and 2.2 mA of current. The distribution is apparently constant downstream of Q35, apart from the possible loss of a small amount of beam. The emittance drops somewhat from Q4 to Q35, but is constant through the remainder of the lattice.

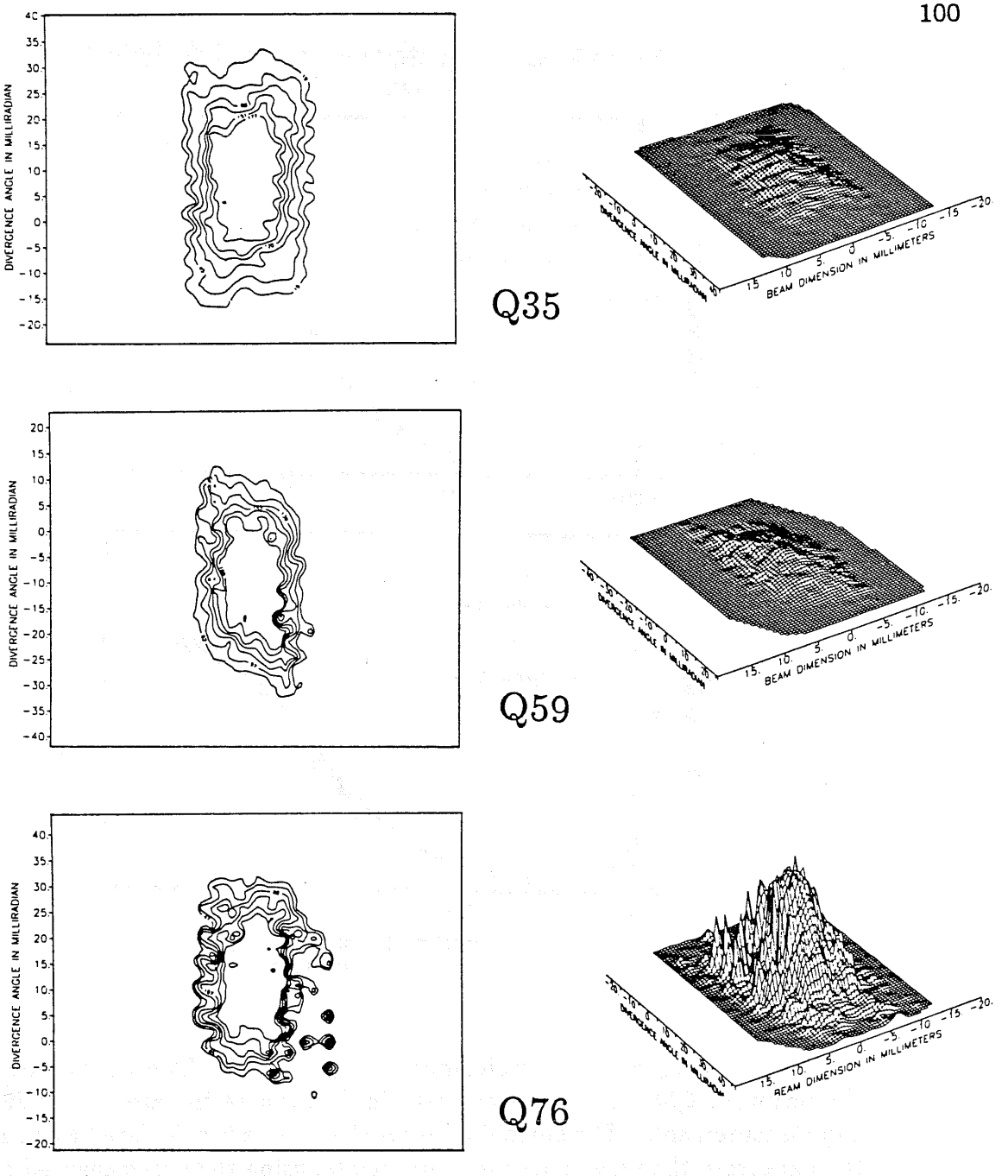

XBL 865-1745

Figure 5.23: Phase space contours for $\sigma_0 = 134°$. The data shown are, by row, for Q35, Q59, and Q76. The appearance of the Q35 and Q59 plots is similar, with no sign of a structured instability. The plots for Q76 show the effect of pulse-to-pulse variation of the beam, noticeable only for the rightmost portion of the beam, as displayed in the contour plot. See the text for more information. The emittance calculated for the beam is insensitive to the few spurious points, and the constancy of the beam distribution downstream from Q35 is evidenced by the data.

radian. This is consistent with loss of beam due to clearance limitations. The values of emittance measured at Q59 and Q76 were, respectively, $1.6 \times 10^{-7}\pi$ meter radian and $1.7 \times 10^{-7}\pi$ meter radian.

In addition, we injected the full 10-mA beam current into the SBTE for $\sigma_0 = 134°$, using the emittance grids set to 8 kV bias ($\epsilon \simeq 3.4 \times 10^{-7}\pi$ meter radian), and we were able to tune the matching section to deliver 5 mA of current to the Faraday cup at Q82, with an emittance of $3.2 \times 10^{-7}\pi$ meter radian. The overall ratio of emittance to current for this output beam is almost identical to that for the 2.7-ma output case discussed above.

Just as for $\sigma_0 = 134°$, we injected the full beam current of 10 mA into the SBTE with $\sigma_0 = 145°$, but using the emittance grid bias set to 7 kV to raise the injection emittance to about $3.2 \times 10^{-7}\pi$ meter radian, and we obtained 4.6 mA at Q82, with an emittance measured at Q76 of $2.8 \times 10^{-7}\pi$ meter radian. The data are shown in Figs. 5.24 and 5.25. From Fig. 5.24 we see that the beam has not reached a completely stable configuration by the time it passes Q59.

For the same 3.4-mA injection current used for the $\sigma_0 = 134°$ case discussed above, but with $\sigma_0 = 145°$, we measured the current at the Q82 cup to be 2.5 mA, with an emittance at Q76 of $2.2 \times 10^{-7}\pi$ meter radian. The ratio of emittance to current for the 4.6-mA beam is about 35% below that for the 2.5-mA output case. In this parameter regime, however, the difference in the derived values for σ is only about 10%. The two output beams are compared in Fig. 5.26.

5.4 Discussion for $\sigma_0 \sim 90°$

The empirical instability region begins at the same lattice strength for which the envelope equations can become unstable, that is, $\sigma_0 \simeq 90°$. However, detailed comparison of the data with envelope instability predictions

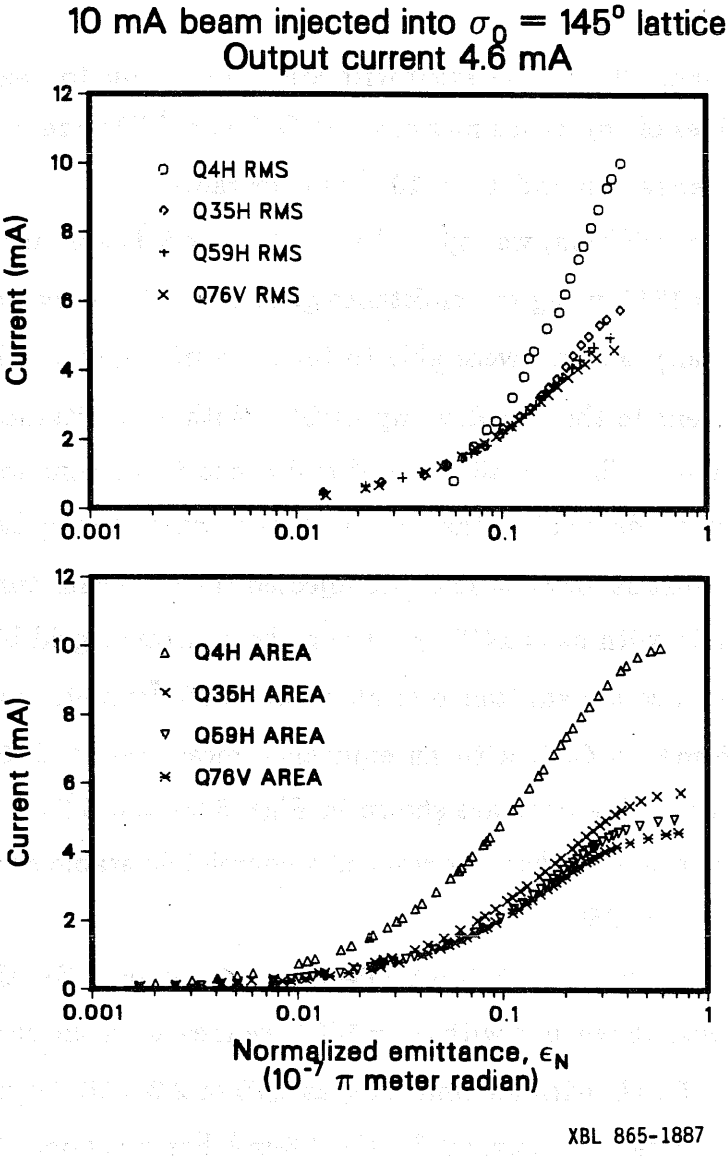

Figure 5.24: Current vs. emittance for $\sigma_0 = 145°$. The beam current at injection is 10 mA, and the emittance has been raised to about $3 \times 10^{-7}\pi$ meter radian by means of the emittance grids. There is a large change in the beam distribution between Q4 and Q35, with more gradual changes in the beam occurring along the lattice. The beam does not quite reach stability before it exits the experimental channel, although the rate of change of the distribution is low.

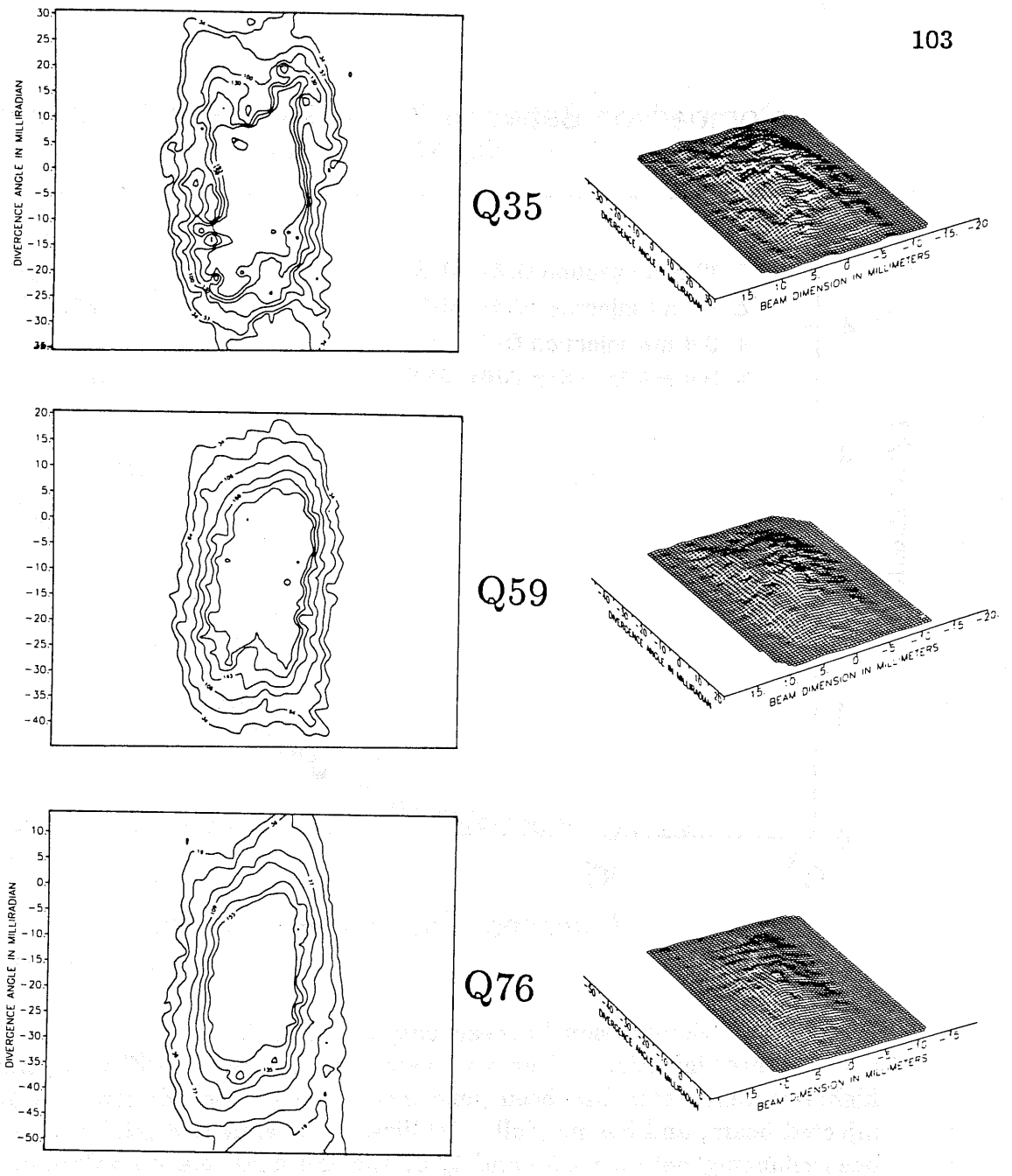

XBL 865-1744

Figure 5.25: Phase space contours for $\sigma_0 = 145°$. These plots are, from top to bottom, for measurements at Q35, Q59, and Q76. The Q35 plots show some structure, similar to, but not as prominent as, that in Fig. 5.21. The grid bias used to spoil the emittance at injection for this sequence of data is 7 kV.

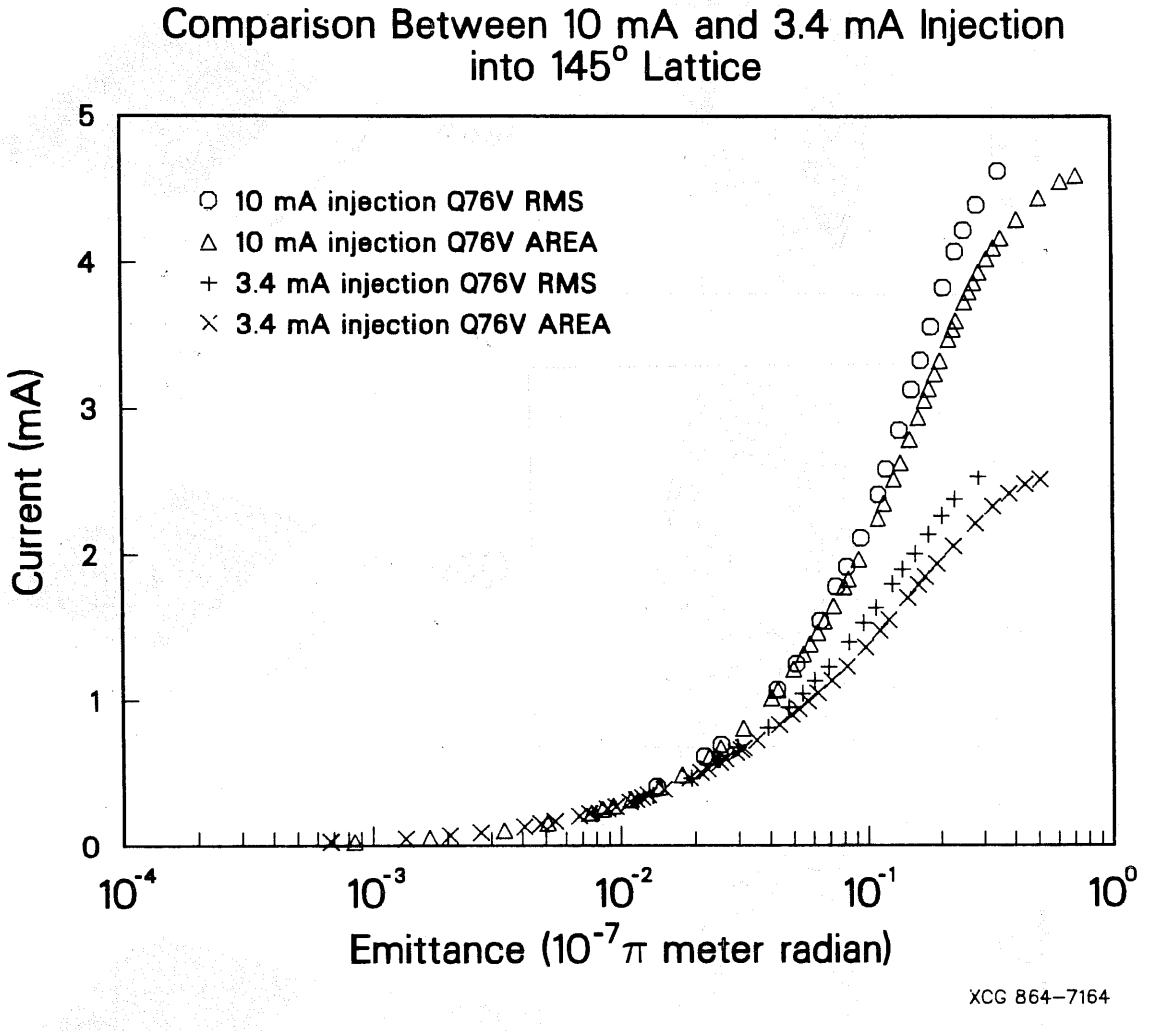

Figure 5.26: Comparison between output beams for $\sigma_0 = 145°$ for 10 mA and 3.4 mA injection. The two cases are somewhat different, but the higher-current beam has been generated through degradation of a 10-mA injected beam, and has not fully stabilized. The emittance and current have been changing between Q59 and Q76, and the final relative values of emittance and current may be very close. The figure is shown as an example of obtaining much higher current at Q82 by injecting an unstable beam, than could be provided by injecting a lower-current, more stable beam.

shows several points of difference:

- The beam shows unstable behavior for parameters for which the "infinitely long" beam, far from the beam ends, is far from the calculated region of envelope instability, with a value of σ too low for instability by factors of 2–4.

- While the calculated growth rates of the envelope instability are small until σ_0 is raised above 100°, the beam shows rapid emittance degradation for σ_0 near 90°.

- The beam stabilizes at an emittance for which the beam remains on the high-intensity side of the instability band.

The maximum growth rates for the envelope instability as a function of σ_0, calculated using the techniques of Laslett [16], by perturbation of the envelope equations, are shown in Fig. 5.27. This calculation was for hard-edge quadrupoles with an occupancy factor of 0.5, but the results are insensitive to the quadrupole occupancy factor. Comparison with calculations both for a thin lens lattice and for the SBTE focusing field representation given in Appendix D shows a difference of only about 1° in σ for the instability thresholds, and nearly identical peak growth rates. Simulation studies have been done by Haber [47] for a low-emittance beam, passing through a lattice set to $\sigma_0 = 90°$. As the current was slowly ramped up (and σ dropped), the emittance increased only after the beam passed a threshold intensity corresponding to $\sigma \simeq 30°$. Our experimental value for the limiting σ for $\sigma_0 = 90°$ is about 25°, as shown in Fig. 5.11.

The evolution of unstable beams as shown in the i vs. $\epsilon(i)$ plots displays some interesting behavior. For $\sigma_0 = 94°$, the beam degrades significantly in only 15 periods, as shown in Figs. 5.28 and 5.29, although the growth

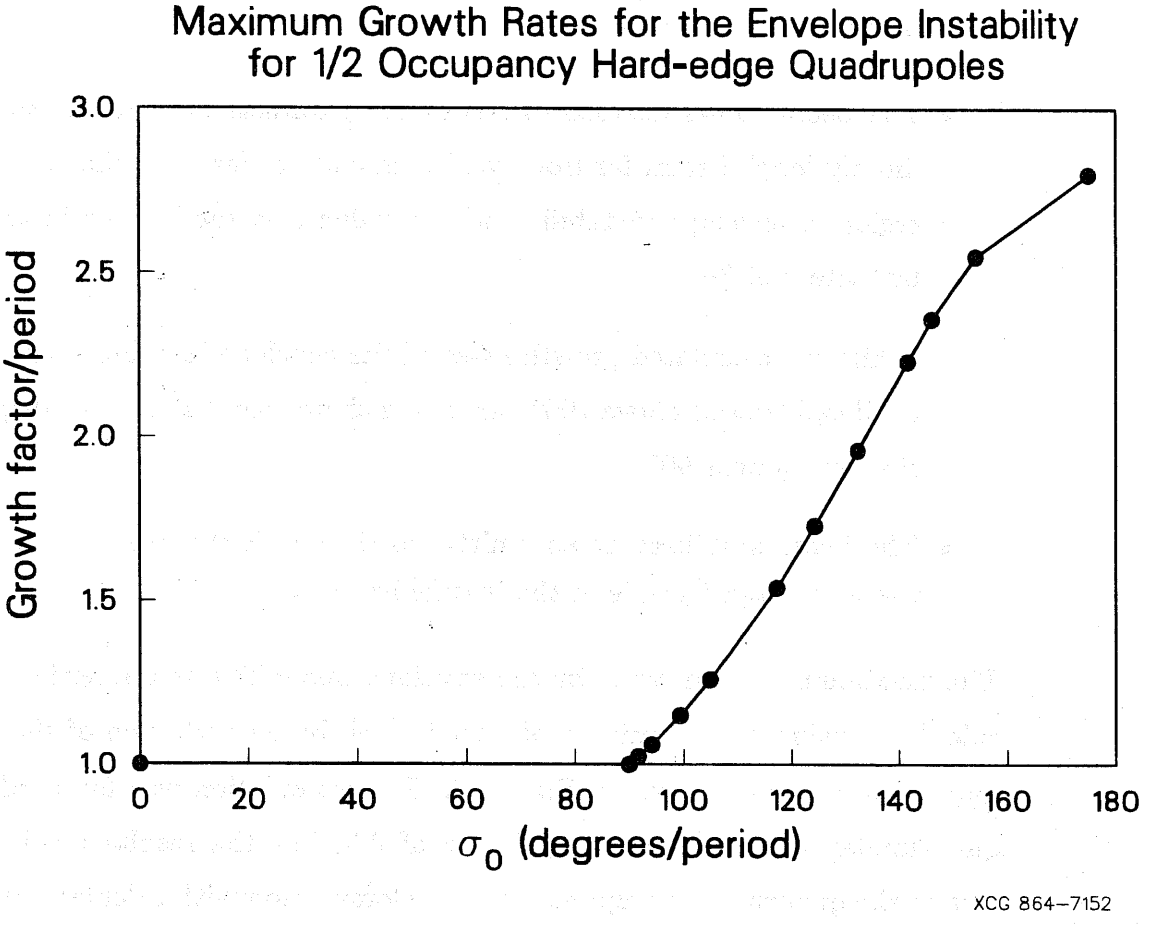

Figure 5.27: Maximum growth rates for the envelope instability for hard-edge quadrupoles with an occupancy factor of 0.5. The thresholds and growth rates were compared with both thin lens quadrupoles and the SBTE model given in Appendix D, and gave agreement within about 1° in thresholds and a few percent in growth rate.

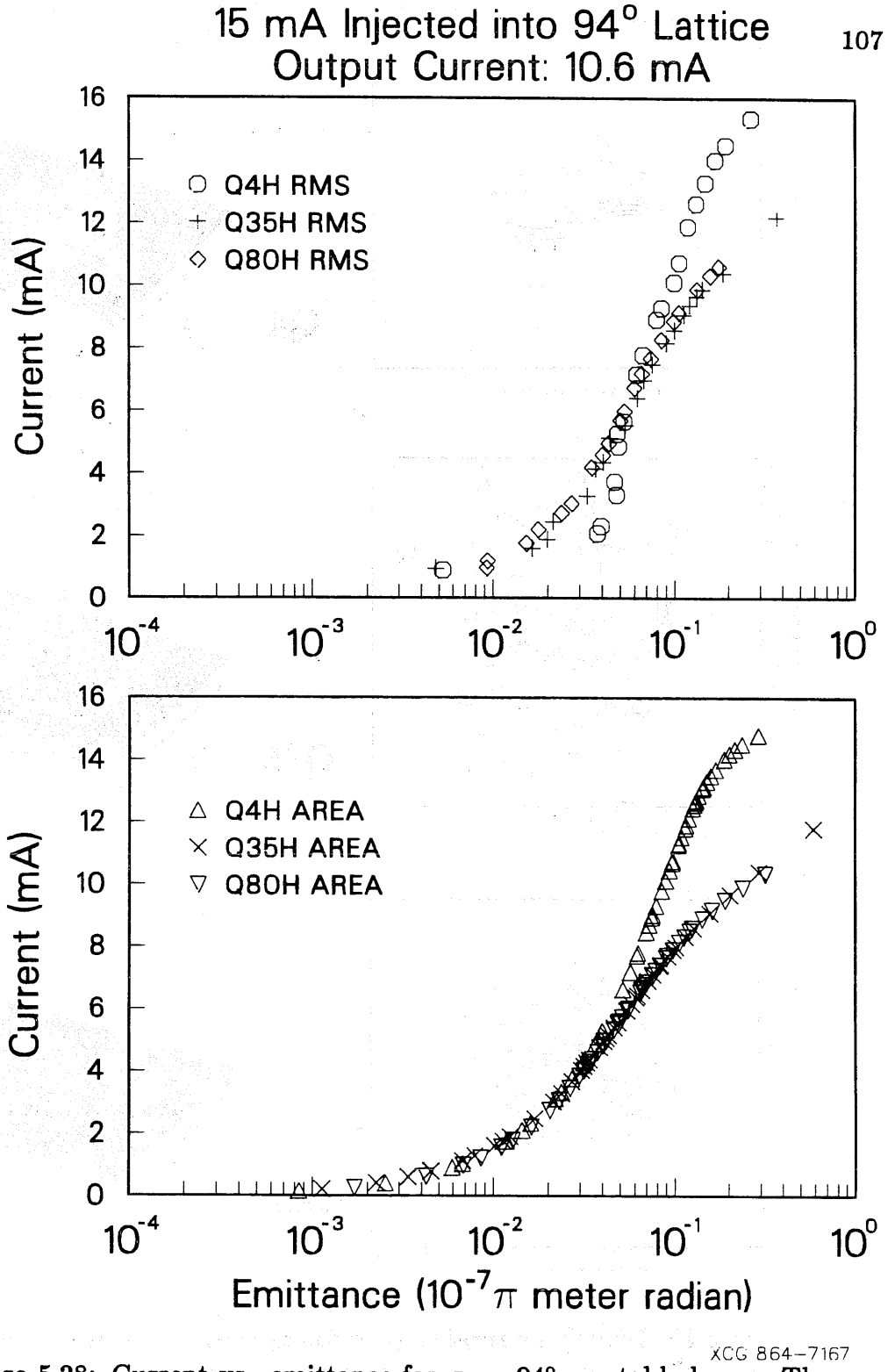

Figure 5.28: Current vs. emittance for $\sigma_0 = 94°$, unstable beam. The core of the beam is little affected during the instability. Most of the change takes place in the outer phase space areas, with the change nearly complete by Q35. Downstream of Q35, the only change is an additional loss of about 2 mA of beam from the phase space tails.

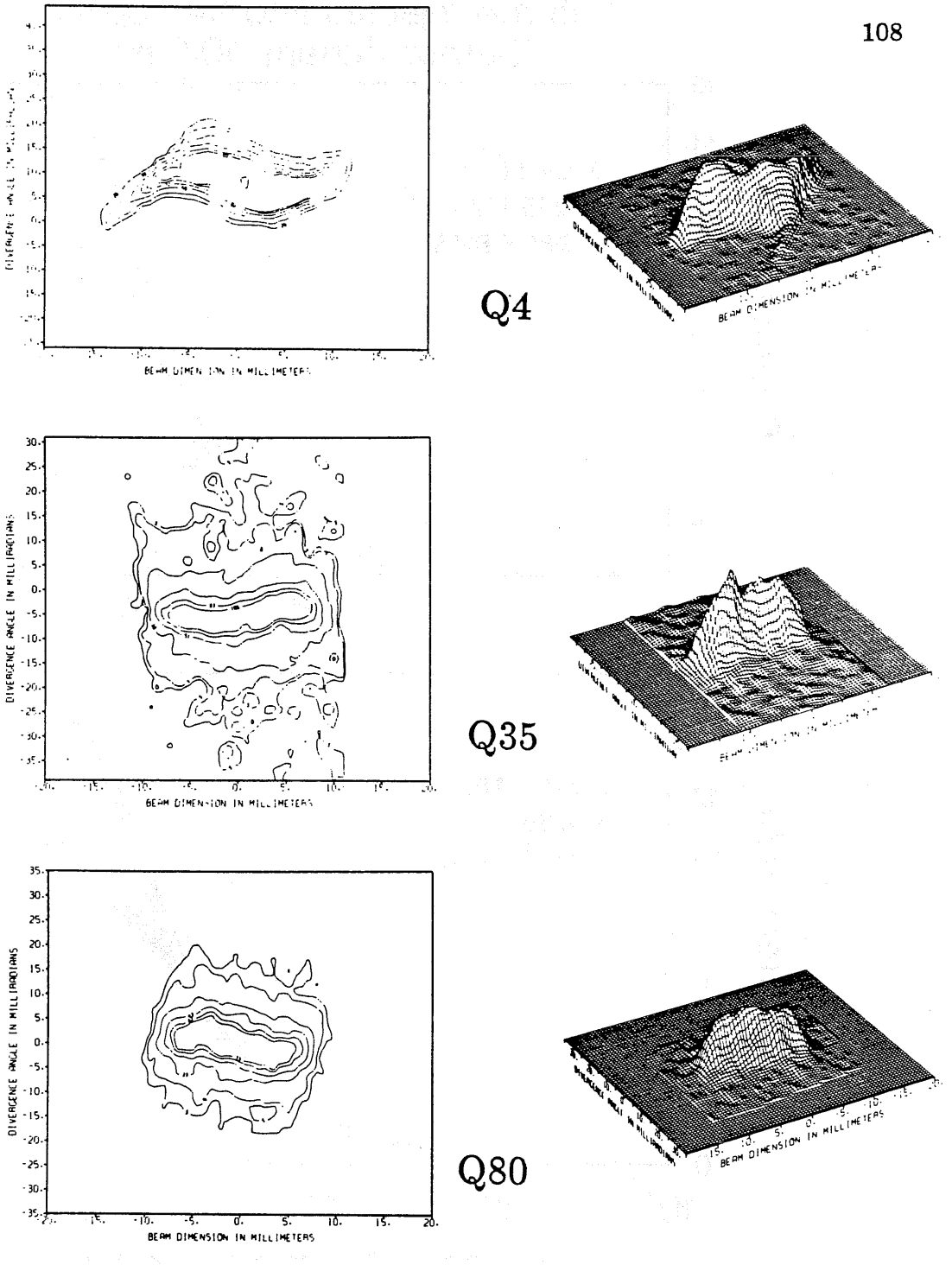

XBL 865-1831

Figure 5.29: Unstable beam behavior for $\sigma_0 = 94°$. The beam has lost about 2.5 mA of the initial 15 mA by the time it reaches Q35. Extensive tails in phase space have developed, which are shed as the beam progresses on to Q80.

rate of the instability near this value of σ_0 is only $4.3 \pm 1.9\%$ per focusing period. This instability is in RMS radius, not in emittance, and the emittance should remain constant until the instability saturates through some nonlinear mechanism. Though the ends of the beam might be near the region of the envelope instability, the value of σ for the bulk of the beam was a factor of at least three below the instability band for this particular mode, yet the beam emittance and current were rapidly degraded. After the initial gross disturbance to the beam, which occurred during the first 15 lattice periods, subsequent measurements indicated that the beam almost exclusively lost particles in the fringes of the phase space distribution. The initial current was 15.2 mA, and the final current was 10.6 mA at the Q82 Faraday cup.

5.5 Discussion for σ_0 much greater than 90°

For $\sigma_0 \geq 118°$, the beam stabilizes with an emittance significantly above that required to guarantee envelope stability, by a factor of 1.8 for $\sigma_0 = 134°$. Recall that σ increases monotonically with ϵ. We found that when we injected too low an emittance, the resulting output emittance overshot the stability threshold, with loss of beam if the aperture clearance was insufficient. Upon raising the injection emittance, the output emittance decreased, with any beam loss diminishing at the same time. Increasing the injection emittance beyond the point at which the injection and output values met caused the output emittance to rise again, as expected.

For $\sigma_0 \geq 134°$, we were unable to transport even 3.5 mA through the entire lattice with no loss of beam. We were able to limit the beam loss to about 20% for $\sigma_0 = 134°$ with a 3.4 mA beam, this loss occurring within the first 15 periods of transport. The beam distribution was stable over the remaining 22 periods of transport for this case, with a measured output current of 2.7 mA. For $\sigma_0 = 145°$, the beam loss was slightly greater for the same injection

conditions. The output current was 2.5 mA, with a total emittance of about $2.8 \times 10^{-7}\pi$ meter radian and with an emittance for the central 95% of the beam of about $2.4 \times 10^{-7}\pi$ meter radian.

When plotted using the parameters σ_0 and σ, the empirical stability boundary is fit closely by a hyperbola of the form

$$\sigma^2 = \sigma_0^2 - const.$$

From smooth-focusing lattice solutions to matched beams, using the K-V distribution, we find a similar relation between σ and σ_0, derived from Eqn. 2.7

$$\sigma^2 = \sigma_0^2 - \frac{1}{2}\left(\frac{180^\circ}{\pi}\frac{2L}{v_z}\omega_p\right)^2, \tag{5.3}$$

where

$$\omega_p^2 = \frac{nq^2}{m\epsilon_0}.$$

Here, n the number density of the beam, q the particle charge, and m the particle mass. The constant value for ω_p which gives a good fit to the empirical stability boundary is given by

$$\omega_p \simeq \frac{2\pi}{3}\frac{v_z}{2L},$$

corresponding to one plasma wave oscillation while the beam transits three lens periods. Using this value in Eqn. 5.3, the x-intercept occurs for $\sigma_0 = 120^\circ/\sqrt{2} \simeq 85^\circ$. Whether this correlation is indicative of a limiting beam "plasma frequency", we cannot definitively answer. However, we have estimated values for the beam density on the axis from our data by the following procedure.

In the low-emittance limit, there is little difference between the current profiles calculated from the K-V (uniform beam) model and from solutions for

a Maxwellian beam distribution (see Eqn. 5.1) for a smooth-focusing channel. For hot beams, however, the current profiles of a K-V beam and a Maxwellian beam are quite different. The Maxwellian has a local current density peaked at the beam axis, while the K-V beam retains its uniform current density. The current density for a uniform density circular beam may be calculated from the projection onto one spatial dimension as

$$J_U = \frac{I}{4\pi\tilde{x}^2}.$$

For a Maxwellian beam in which the self-field is not dominant over the emittance term in the envelope equations, the distribution in real space takes the Gaussian form

$$n(x) \propto \exp\left(\frac{-x^2}{2\tilde{x}^2}\right),$$

where $\tilde{x}$ is the RMS radius in the x dimension. For this distribution, the peak current density (on-axis) is twice that for a uniform distribution with the same current and RMS beam radius

$$J_G = \frac{I}{2\pi\tilde{x}^2}.$$

We will take these two expressions, J_U and J_G, as estimates for bounds on the peak current density of our beams for the $\sigma_0 > 100°$ region with emittances high enough to bring the beam out of the space-charge dominated regime. The results are shown in Fig. 5.30. In the range $\sigma_0 < 88°$, the beam emittance is very low and the current density in the beam should be very close to uniform. In this region, the current density will fall along the line calculated for ideal lattices and low transverse kinetic energy. However, for $\sigma_0 > 120°$, for which the emittance term in the envelope equations is much higher relative to the current term than for low-σ_0, the beams may be expected to be

nearly Gaussian in profile because of the dominant effect of the emittance in the envelope equations. In this approximation, the beam parameters are consistent with having a number density limited by a fixed value. There is, of course, a transition region between the two extremes. While this is by no means compelling evidence, it is consistent with the empirical relation between σ and σ_0 found in our experiments.

5.6 Summary of Results

We have measured the emittance and current of a beam with intense space-charge fields, at various positions along a quadrupole channel consisting of 41 FODO periods, plus five matching lenses. and have characterized the empirical limits of stability, defined empirically as the conservation of the beam current and emittance along the channel. We have summarized the results graphically in Fig. 5.11 in terms of the quantities σ_0 and σ. We also present these same data in terms of σ_0 and the ratio σ/σ_0 in Fig. 5.31, compared with the early conjecture by Maschke and the later estimate by [HHLS] of possible limiting values of the quantity σ/σ_0.

1. For low focusing strength ($\sigma_0 < 88°$) we have observed no collective limit to low-emittance beam transport in an A.G. lattice. Our source has an intrinsic minimum emittance, which places a lower bound on the value of σ accessible at a given lattice strength. The only increase in emittance we have observed in the SBTE for $\sigma_0 < 88°$ has been associated with aberrations in the phase space distribution of the beam, which were dependent on the matching section configuration. We believe that the matching section field is responsible for these aberrations, rather than any collective beam interaction with the lattice. (Interaction of the beam with the lattice through induced charge on nearby conductors provides measurable effects on the beam (see section 6.2),

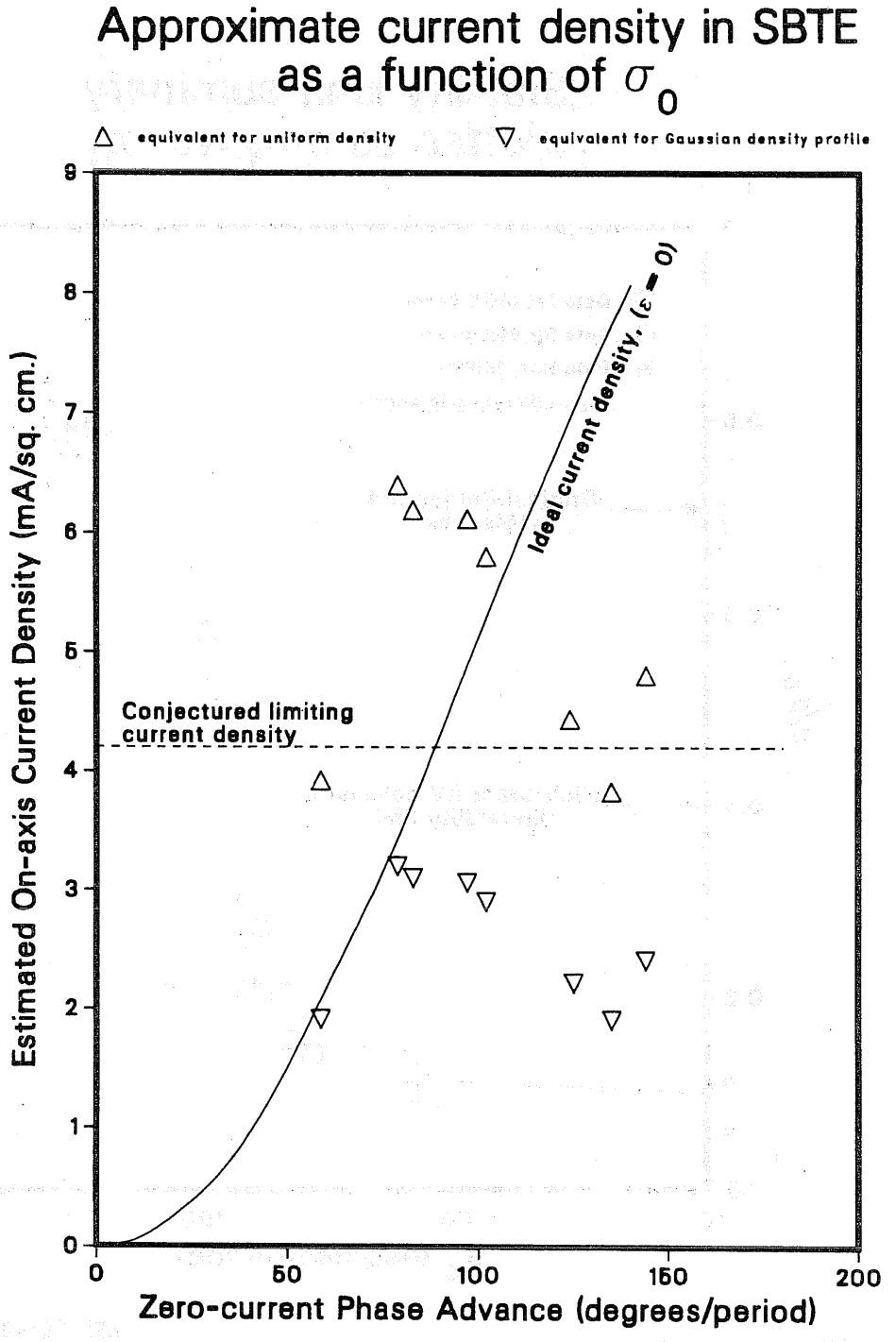

Figure 5.30: Bounds for peak current density of the beam near the stability boundary. For $\sigma_0 \leq 88°$, the beam is cold enough to treat in the uniform density limit, in which the current density is $I/4\pi\tilde{x}^2$. For $\sigma_0 \geq 124°$, however, the emittance dominates, and the beam is better approximated as Gaussian in current density. In this limit, the peak current density of the beam is $I/2\pi\tilde{x}^2$. We have plotted these two quantities for the beam parameters listed in Table 5.1. See text for discussion.

XBL 865-1760

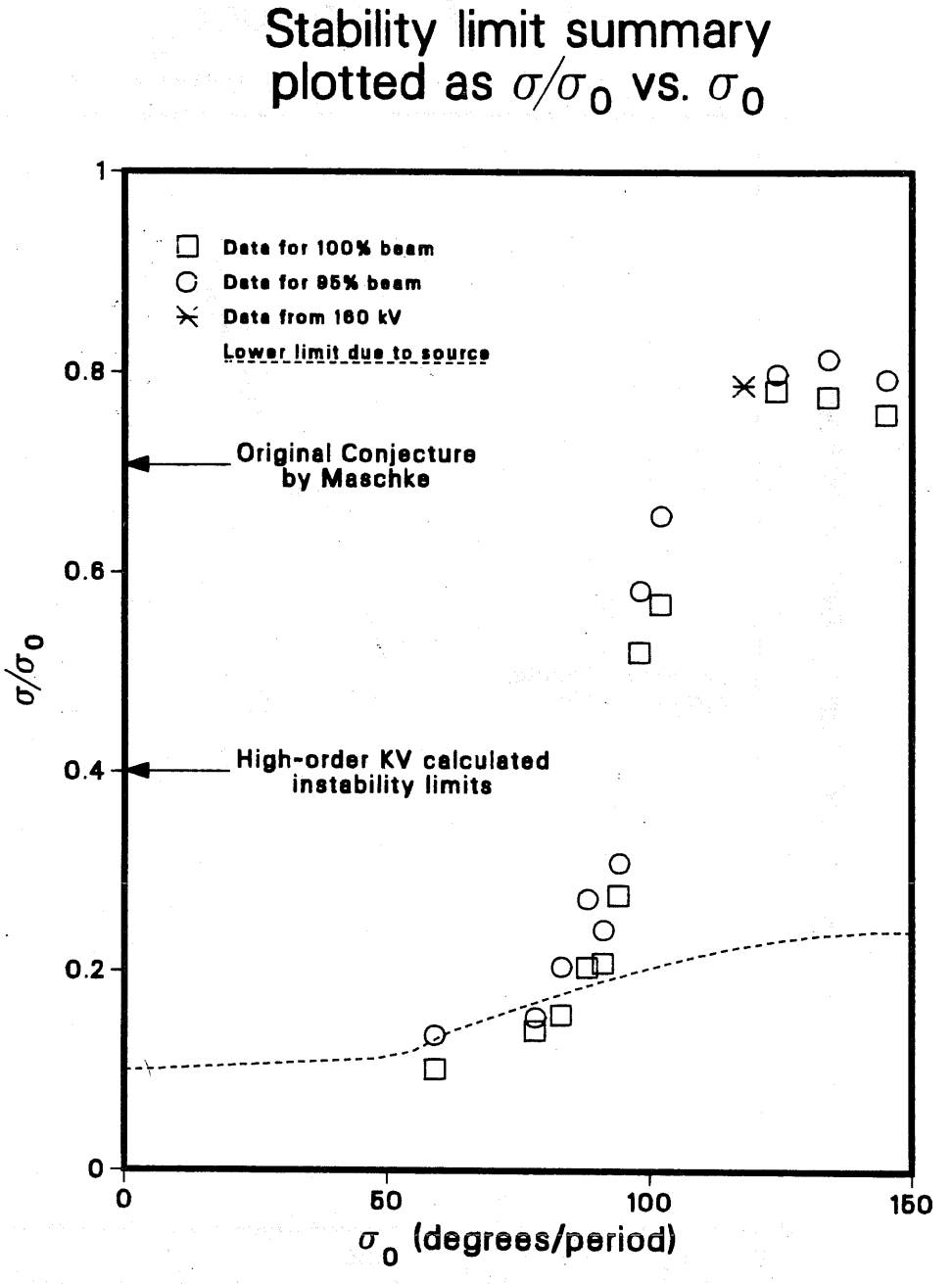

Figure 5.31: Results of the stability measurements from the SBTE using the parameters σ/σ_0 and σ_0. The early conjecture by Maschke ($\sigma/\sigma_0 \geq 0.7$) underestimates the beam intensity attainable in the SBTE. The later estimate ($\sigma/\sigma_0 \geq 0.4$), based on results for K-V beams [20], is also somewhat conservative for $\sigma_0 < 88°$. In this region, our lower limit on the attainable value of σ/σ_0 is given by the intrinsic emittance of the SBTE ion source, rather than by collective effects. See the text for more discussion.

and this mechanism may provide the practical low-ϵ limit on space-charge dominated beam transport.)

2. For $\sigma_0 > 88°$, we observed intensity-dependent beam degradation. The mechanism is not certain, and we have seen definite structure in the phase space distribution of the beam to signal a particular mode of instability only for $\sigma_0 = 98°$ and $\sigma_0 = 102°$. In the unstable behavior in simulation work [45,46], such structures are time-dependent, and we may have measured the beam distribution at an unfortunate choice of points along the channel. It is more probable, however, that we have not seen these mode structures because in the measurements we have made, we have generally attempted to inject the beam with parameters for which we expect only mild instability.

3. When we reach $\sigma_0 = 88°$ without attenuating our beam, we find a small beam loss ($\sim 4\%$). Further increases in σ_0 result in a dramatic increase in the emittance of the beam and much greater loss of current. This threshold in σ_0 for growth of the beam emittance corresponds fairly closely to the threshold strength for envelope instability, but the detailed beam behavior is not consistent with this as the limiting phenomenon. The beam becomes unstable for parameters well outside the intensity band for the envelope instability and stabilizes while remaining on the high-intensity side of the unstable band. The growth rates calculated from perturbation of the envelope equations are inconsistent with the rapidity of the observed beam degradation in the neighborhood of $\sigma_0 \sim 90°$. For $\sigma_0 > 118°$, the beam became stable only for an emittance much greater than that required to bring the beam to the low-intensity side of the envelope instability band, by a factor of about 2 for $\sigma_0 \geq 134°$.

4. Although our experimental data are not well-correlated with the envelope stability curve, they are well represented by the smooth approximation relation

$$\sigma^2 = \sigma_0^2 - \frac{1}{2}\left(\frac{180^\circ}{\pi}\frac{2L}{v_z}\omega_p\right)^2,$$

where $2L\omega_p/v_z$ is a constant approximately equal to $2\pi/3$. This is the hyperbola plotted along with the data. The x-intercept of this curve is at $120^\circ/\sqrt{2} \simeq 85^\circ$. For emittances corresponding to values of σ and σ_0 below this curve, there is a violent instability in the phase space distribution of the beam. We present this as an observation on the beam parameters correlated with the cessation of this violent instability. We find no significant growth of emittance for values of σ and σ_0 above this curve within the available transport channel length (82 quadrupoles plus the 5 matching lenses), with the exception of the region bounded by the instability curves for the envelope mode in Fig. 5.11.